# Location of microseismic swarms induced by salt solution mining

J. Kinscher,[1] P. Bernard,[2] I. Contrucci,[1] A. Mangeney,[2] J.P. Piguet[3] and P. Bigarre[1]

[1]*L'Institut National de l'Environnement Industriel et des Risques INERIS, Nancy, France. E-mail: j.l.kinscher@gmail.com*
[2]*Institut de Physique du Globe de Paris IPGP, Paris, France*
[3]*École des Mines de Nancy - Université de Lorraine, Nancy, France*

**SUMMARY**

Ground failures, caving processes and collapses of large natural or man-made underground cavities can produce significant socio-economic damages and represent a serious risk envisaged by the mine managements and municipalities. In order to improve our understanding of the mechanisms governing such a geohazard and to test the potential of geophysical methods to prevent them, the development and collapse of a salt solution mining cavity was monitored in the Lorraine basin in northeastern France. During the experiment, a huge microseismic data set (∼50 000 event files) was recorded by a local microseismic network. 80 per cent of the data comprised unusual swarming sequences with complex clusters of superimposed microseismic events which could not be processed through standard automatic detection and location routines. Here, we present two probabilistic methods which provide a powerful tool to assess the spatio-temporal characteristics of these swarming sequences in an automatic manner. Both methods take advantage of strong attenuation effects and significantly polarized *P*-wave energies at higher frequencies (>100 Hz). The first location approach uses simple signal amplitude estimates for different frequency bands, and an attenuation model to constrain the hypocentre locations. The second approach was designed to identify significantly polarized *P*-wave energies and the associated polarization angles which provide very valuable information on the hypocentre location. Both methods are applied to a microseismic data set recorded during an important step of the development of the cavity, that is, before its collapse. From our results, systematic spatio-temporal epicentre migration trends are observed in the order of seconds to minutes and several tens of meters which are partially associated with cyclic behaviours. In addition, from spatio-temporal distribution of epicentre clusters we observed similar epicentre migration in the order of hours and days. All together, we suggest that the recorded microseismicity mainly represents detachment and block breakage processes acting at the cavity's roof, indicating a zone of critical state of stress and where partial fractures cause chain reaction failures as a result of stress redistribution processes.

**Key words:** Controlled source seismology; Earthquake dynamics; Seismic monitoring and test-ban treaty verification; Earthquake interaction, forecasting, and prediction; Body waves; Seismic attenuation.

## 1 INTRODUCTION

Natural or man-made underground cavities, particularly when they are shallow, can provoke large-scale land subsidence and collapses accompanied by catastrophic social-economic impacts. The potential of passive microseismic monitoring to prevent such disasters is world widely discussed and is routinely used in the active mining sector (e.g. Young *et al.* 1992; Mendecki 1996; Senfaute *et al.* 1997; Urbancic & Trifu 2000; Li *et al.* 2007; Gibowicz 2009; Hudyma & Potvin 2010). To provide reliable seismic prediction of a large-scale ground failure, local and continuous measurements are generally required in order to sufficiently resolve the associated mechanisms and evolution stages of the cavitation system. Up to now, only few examples in literature can be found documenting local microseismic monitoring of natural (Wust-Bloch & Joswig 2006; Malovichko *et al.* 2010; Dahm *et al.* 2011) or man-made (Malovichko *et al.* 2009; Trifu & Shumila 2010) underground caving systems and collapses. The most advanced use of microseismic monitoring with respect to caving processes is found in block or panel caving operations in mines where microseismicity is conventionally used for tracking the cave propagation (e.g. Duplancic & Brady 1999; Glazer & Hepworth 2005; Wuestefeld *et al.* 2011).

In this context, microseismic and other geophysical monitoring tools were applied to a salt cavity that was created by salt dissolution mining (a SOLVAY exploitation) as part of a large multiparameter research project founded by the research 'group for the impact and safety of underground works' (GISOS, http://gisos.ensg.inpl-nancy.fr/gisos-info-en/gisos-info-en/) at Cerville-Buissoncourt in Lorraine, France (Mercerat 2007; Klein *et al.* 2008; Cao *et al.* 2010; Daupley *et al.* 2010; Mercerat *et al.* 2010; Contrucci *et al.* 2011; Lebert *et al.* 2011). The continuous growth of the cavity was monitored from 2004 until 2009, when the cavity reached its critical size and a 'controlled' collapse was initiated by brine pumping. This experimental project provides a unique opportunity to evaluate the potential of microseismic monitoring and mechanical models with respect to a growing and collapsing cavity system in a salt solution mining environment (e.g. Daupley *et al.* 2005), and similar 'prone to collapse' scenarios as in evaporite mines (e.g. Whyatt & Varley 2008) or natural sinkhole systems in karstic (e.g. Caramanna *et al.* 2008) and evaporitic (e.g. Gutierrez *et al.* 2008) terrains. In addition, the final cavity collapse of Cerville-Buissoncourt was also discussed with respect to remote triggering by a large distant earthquake (Jousset & Rohmer 2012).

Initial analysis of the obtained microseismic data set implied various applications of body wave phase-based routine tools for microseismic event detection and location (Mercerat 2007; Klein *et al.* 2008; Cao *et al.* 2010; Mercerat *et al.* 2010; Contrucci *et al.* 2011) as they are commonly used in global seismology and industrial monitoring, for example in mines or geothermal or hydrocarbon reservoirs (e.g. Lay & Wallace 1995; Warpinski 2009, Zang *et al.* 2014, and references therein). However, similarly to other local passive microseismic studies of 'prone to collapse' scenarios (e.g. Mertl & Bruckl 2007; Spillmann *et al.* 2007; Levy *et al.* 2010), only a minor portion of the whole microseismic data set could be successfully treated using routine analysis tools (in our case ~20 per cent). General problems of accurate body wave phase picking are related to high attenuation effects, partial lack of *S*-wave phases due to unusual source characteristics or near field effects, *P*-to-*S* wave conversions associated with strong velocity contrasts, emergent *P*-wave onsets, and precursory signals ahead of impulsive *P* waves. Next to these particularities, major portions of the Cerville-Buissoncourt microseismic data set (~80 per cent) are represented by unusual swarming sequences similar to 'multiple events' introduced by Mertl & Bruckl (2007), and Spillmann *et al.* (2007). These swarming sequences are formed by microseismic events that superimpose to dense and complex event clusters and where *P*-wave onsets are often covered by the coda of the preceding events. Moreover, the total volume of the microseismic data set comprises around 50 000 event files what generally require automatic data processing, as manual phase picking is very time consuming.

Here, we present two new automatic location methods aimed to resolve the spatio-temporal characteristics of the recorded swarming sequences at first order. Both methods take advantage of the dominance of *P*-wave energies at higher frequencies resulting from strong *S*-wave attenuation. The first method uses simple signal amplitude estimations for different frequency bands, combined with an attenuation model to constrain the hypocentre location. Amplitude-based location was introduced by Battaglia & Aki (2003) and was so far applied to volcanic environments (e.g. Yamasato 1997; Jolly *et al.* 2002; Battaglia *et al.* 2005; Di Grazia *et al.* 2006; Taisne *et al.* 2011), and icequakes (Jones *et al.* 2013). The second method is designed to locate microseismic sources based on the identification of significantly polarized high frequency *P*-wave energies and their corresponding polarization angles for three-component stations. The location results for both methods are formulated in a probabilistic manner and can be combined to solve the location problem. Both approaches and their combinations are evaluated using a microseismic data set recorded during a crisis in 2008 that was associated with a period of significant cavity growth.

This paper is organized as follows: in Section 2, the study site and the microseismic network are briefly introduced. In addition, some of the major microseismic signal characteristics are described with respect to a training data set which is generally used to calibrate and evaluate the design and potential of the developed location methods, which are later presented in Section 3. Section 4 discusses our application results with respect to (i) preselected seismic events of well constrained hypocentres, (ii) swarming sequences and (iii) the 2008 microseismic crisis.

## 2 DATA SET DESCRIPTIONS

### 2.1 Experimental setting

At Cerville-Buissoncourt, northeastern France, the geological setting is constituted of subhorizontal Triassic submarine sequences: a marly-sandy layer (0–119 m depth), a thin but competent (stiff) Dolomite layer known as the Beaumont Dolomite (119–127.5 m depth), a poorly consolidated layer of anhydritic Marls (127.5–183.5 m depth), and the salt deposit which reaches its final depth at 348 m (Fig. 1). The salt deposit is exploited by solution mining by means of the 'channel and drilling' technique (Fig. 1a, e.g. Mercerat *et al.* 2010; Contrucci *et al.* 2011). The monitored cavity was located at a depth of around 250 m, within the salt layer. Its geometry was initially evaluated using sonar measurements obtained by SOLVAY in 2004, revealing 150–200 m of lateral extensions and a maximum cavity height of around 50 m (Fig. 1). The mechanical stability of the cavity and the overburden is mainly controlled by the elastic strength of the stiff Dolomite layer (Daupley *et al.* 2005). In addition, the cavern was filled with saturated brine, inducing a significant pressure on its walls and on the overburden (~2.0 MPa).

After solution mining was placed in a standby mode from 2004 to 2007 (Mercerat 2007; Mercerat *et al.* 2010), it was resumed in 2007 June by moderate water injections at well cases located 200–300 m further north of the cavity structure (Fig. 1a). In the following period, between 2008 March and May, a significant vertical development of the cavity height, of about 50 m, was recorded by periodic sonar measurements obtained along two profiles (Fig. 1). This cavity growth was mainly associated with the caving process of the poorly consolidated anhydrite Marl layer located above the cavity structure, striking an estimated volume of 500 000 m$^3$ of material.
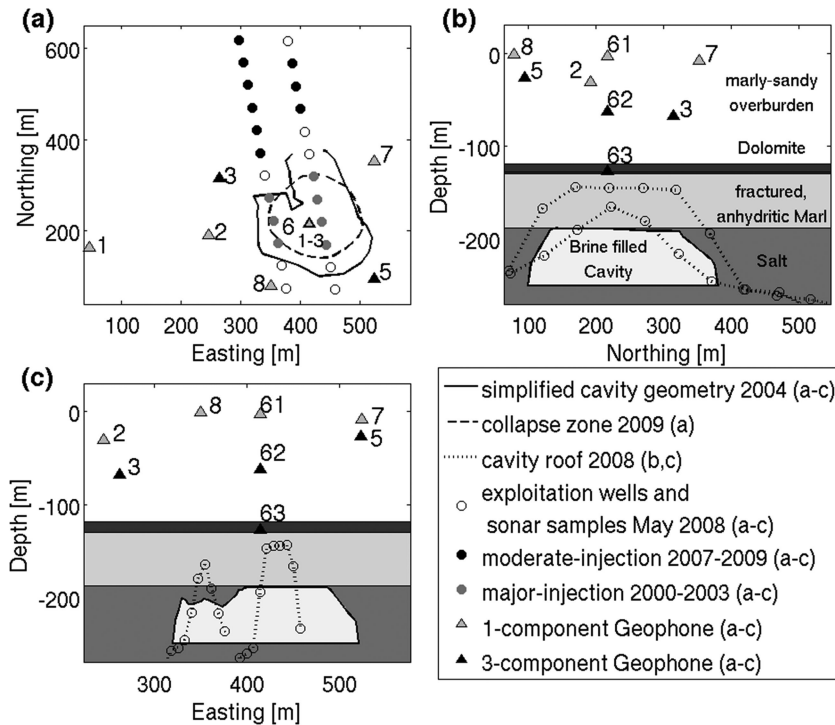
**Figure 1.** Study site. (a–c) The stations (triangles, named by numbers) of the microseismic network, cavity structure, and the major geologic layers. The border of the collapsed cavity area (dashed circle) in 2009 (a) is taken from Lebert *et al.* (2011). Northing and easting are given in metres relative to a reference point X = 892900 m and Y = 116000 m defined by the Lambert 1 Nord (NTF, Paris) coordinate system. (b, c) Sonar measurements (small circles) demonstrate the extension of the cavity roof (dotted lines) after the microseismic crisis in 2008 as compared to the initial cavity roof extension in 2004 (thick black continuous lines). For further references see Section 2.1, respectively.

The microseismic network constituted a high resolution monitoring system of five one-component and four three-component 40 Hz geophones (GS-20DH, Geospace), with a sampling frequency of 5 kHz (Klein *et al.* 2008; Fig. 1). The geophone's frequency response is flat and clean up to 400 Hz, and declines towards lower frequencies below 40 Hz. Due to the considerable number of channels and the high sampling frequency, the acquisition system operated in a triggering mode adjusted to the static background noise level.

## 2.2 First order event classification

The 50 m heightening of the cavity roof in 2008 was accompanied by a clear increase in the seismic activity of around 6000 event files recorded in March, 7000 files recorded in April and around 1000 files recorded in May. Swarming sequences represent around 80 per cent of the recorded data with durations of the order of 5–200 s (Cao *et al.* 2010; Mercerat *et al.* 2010; Contrucci *et al.* 2011). Generally, two types of swarming sequences, detected on all or most stations with variable signal-to-noise ratio, can be classified from visual inspection (Fig. 2): (i) a concatenation of distinguishable single events, which we call hereafter 'isolated events' and (ii) partly interlaced seismic events, which we call 'tremor-like' due to their formal resemblance to spasmodic tremors commonly observed in volcanic environments (e.g. McNutt 1992).

The isolated events generally last 0.1–0.5 s (Fig. 2) and also occur apart from any swarming sequence. They often show clear and impulsive *P*-wave onsets, while *S* waves can only be identified from the three-component stations. On the other hand, the tremor-like swarming sequences are distinguished by their quasi-continuous signals, in such a way that an event appears before the return to the background level of the previous event's coda. Even though individual events in such tremor-like sequences cannot be distinguished or separated, generally *P*- and *S*-wave phases appear to be present (Fig. 2). From the spectrograms shown in Fig. 2, there appears to be no significant difference in the spectral contents of the isolated and tremor-like event sequences, showing a similar frequency range of 20–200 Hz. Nevertheless, owing to the high frequency response of the 40 Hz geophone a reliable examination for lower frequency signal contents (<20 Hz) of the isolated and tremor-like events is not feasible. An indication for the presence of low frequency signal was reported by Jousset & Rohmer (2012) who documented the presence of very similar microseismic swarms associated with a clear long-period (LP) signature in the collapsing period in 2009.

We think that possibly both types of seismic signals, isolated and tremor-like, mainly represent processes of detachment and block breakage at the cavity roof, in the overlying Marl layer and the overburden. Seismic energy released by the impacts of falling blocks on the cavity floor is rather unlikely, since the brine-filled and pressurized cavity should reduce significantly the fall velocity of detached Marl or salt blocks. In addition, the sunken Marl blocks along the cavity floor are widely fractured and brine-saturated, forming an unconsolidated viscous interface which is expected to significantly damp the impacts of falling blocks (e.g. Malovichko *et al.* 2010). As a result, the generation of acoustic emissions from these rather low energy and damped impacts is probably negligible and not detectable by our high frequency
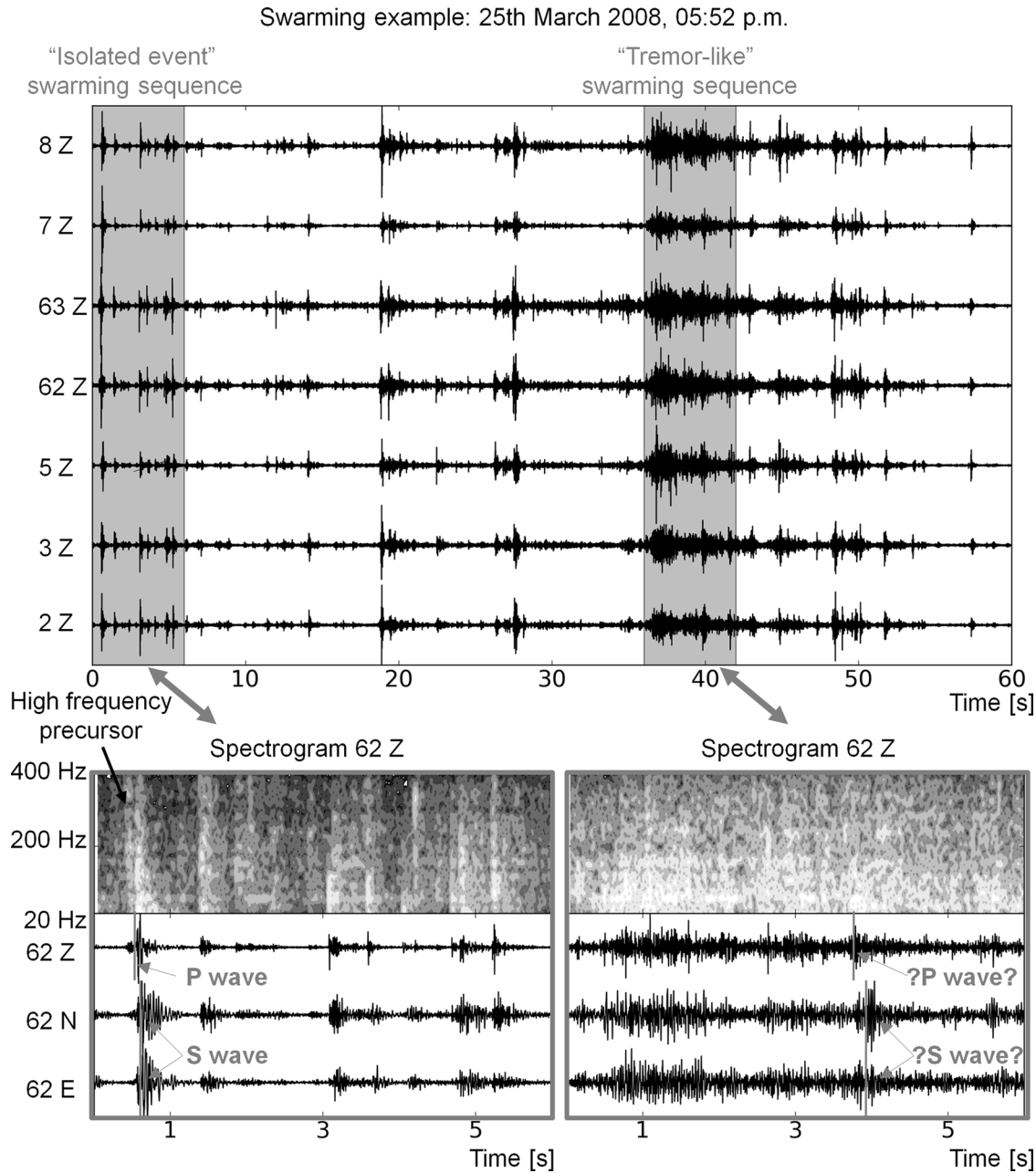
**Figure 2.** Microseismic data example. Example of a typical swarming sequence recorded during the microseismic crisis of 2008. (Upper panel) Seismogram traces for the Z components and examples of isolated event and tremor-like swarming sequences (grey shaded areas). Spectrograms and the three-component traces of station 62 corresponding to the isolated event (left lower panel) and tremor-like sequence (right lower panel). Spectrograms were calculated using a 0.15 s window length with 90 per cent overlap, while intensities are presented in a normalized dB scale for seven distinct contour levels (grey scale).

seismic instruments. It must be stressed that for now this view of breaking and collapsing roof is rather speculative. However, in the following discussion of the location results we will be able to give some more constraints supporting this hypothesis.

### 2.3 Generation and study of a training data set of classically located events

Even though *P*- and *S*-wave phases are generally present in the microseismic data, the application of automatic arrival time based detection and location approaches face strong limitations. Detection of consistent *P*-wave phases, that is *P*-wave phases detected at different station with respect to the same seismic event, is generally impeded by partially emergent *P*-wave onsets as well as *P*-wave onsets covered by the coda of preceding events in swarms or by high frequency precursor signals (Fig. 2) which are not consistently observed from all network stations. Secondly, hypocentral distances are very small (0–300 m) so that picking errors are generally in the same range as traveltimes (Appendix). Moreover, dominant refraction effects as introduced by the high-speed Dolomite layer produce *P–SV* conversions (see Section 2.3.2 and Appendix) rendering consistent *S*-wave phase identification a very challenging task.
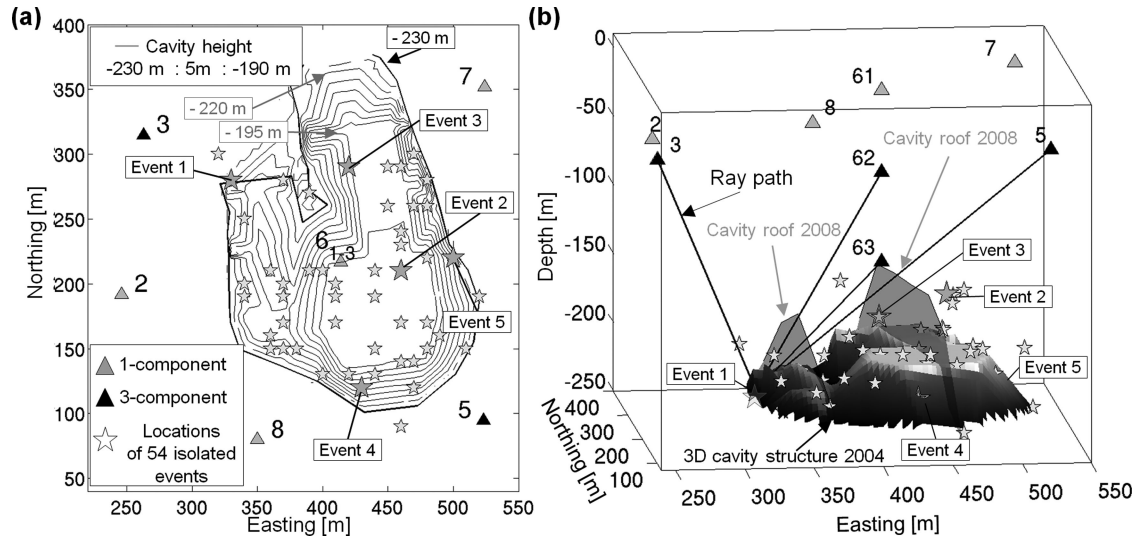
**Figure 3.** Results from classical location for the training set of 54 located isolated events (small stars) (Appendix), used later for the calibration of our location approaches. Numbered larger grey stars mark isolated events partially discussed in more detail in the text. (a) Top view of the 3-D cavity structure shown by the contours (solid black and grey lines). (Right-hand panel) Side view of the 3-D cavity structure determined in 2004, and the cavity growth registered in 2008 (grey shaded areas) (Fig. 1, Section 2.1).

In order to calibrate and evaluate the alternative location approaches proposed in our paper, we first generate a training set of 54 isolated events which were classically located based on *P*-wave polarization angles and clear and impulsive *P*- and *S*-wave arrival times (Figs 3 and 4, Appendix). These located events are homogeneously distributed over the entire cavity zone, and therefore, are supposed to adequately sample the expected variety of source and propagation effects. In the following, we present the major characteristics observed from the training data set which will later help to interpret and better understand the design and functionality of the developed location approaches.

### 2.3.1 Attenuation, scattering and amplification site effects

From the obtained hypocentre locations of the training set (Fig. 3), we find that spectral characteristics of these events clearly reflect attenuation and scattering effects, depending on the source and receiver positions relative to the cavity structure. Such an attenuation effect is observed by comparing the *P* waveforms of event 1, recorded at stations 3 and 62 (Fig. 4), both located at similar hypocentral distances (Fig. 3). The wavefield observed at station 3 did not pass through the cavity structure and therefore the *P*-wave onset appears impulsive and contains significant high frequency energy (Fig. 4). In comparison, the wavefield recorded at station 62 and 63 clearly traversed the cavity structure or the overlying fractured Marl layer, such that its higher frequency content almost vanishes and the *P*-wave onset consequently appears emergent or 'cigar-shaped'. In addition, peak-to-peak *P*- and *S*-wave amplitudes are significantly reduced at the most distant station 5, clearly documenting the presence of strong attenuation effects.

In order to get a rough idea about the frequency content of the microseismic events recorded at each station, we simply represented the spectral characteristics of the 54 isolated events by their smoothed average spectra, calculated for each station (Fig. 5). The average spectra are calculated for the frequency range of 10–1000 Hz, describing the mean spectral amplitudes for each 10 Hz interval. The frequency content from the average spectra is around 20–200 Hz as consistent with the spectrograms shown in Fig. 2. From visual inspection of the different event spectra no significant differences in the frequency contents could be observed. The mean of the relative standard deviation (*RSD*) of the 54 event spectra with respect to the average spectrum at frequencies of 20–200 Hz is similar for all stations and smallest at station 2 *RSD* ∼72 per cent and highest at station 62 *RSD* ∼88 per cent. As a result, it can be concluded that the average spectra represent a relative good first order approximation of the general spectral characteristics of the 54 events.

Next to the frequency content, two other major trends in the spectral characteristics can be seen from the average spectra (Fig. 5). One is the consistently decreasing spectral shape, observed at each station and especially at higher frequencies (>100 Hz), what illustrates the dominance of attenuation effects in the spectral event characteristics. Secondly, the absolute spectral amplitudes at each station are clearly related to the mean hypocentral distance, reflected by the increasing amplitudes at deeper stations (stations 3, 62 and 63) and the decreasing mean seismic energies at stations located along the cavity borders and at shallower depths (stations 2 and 5). At lower frequencies (<100 Hz), clear amplification site effects can be observed at surface stations 7 and 8, probably resulting from resonance inside the unconsolidated soil.

### 2.3.2 Trends in the seismic body wavefield

By analysing simple *P*- and *S*-wave characteristics for the 54 located events at the four three-component stations (3, 5, 62 and 63), we noticed systematic behaviours in the seismic body wavefields (Fig. 6) which are interpreted as a distinct propagation effect introduced by the high
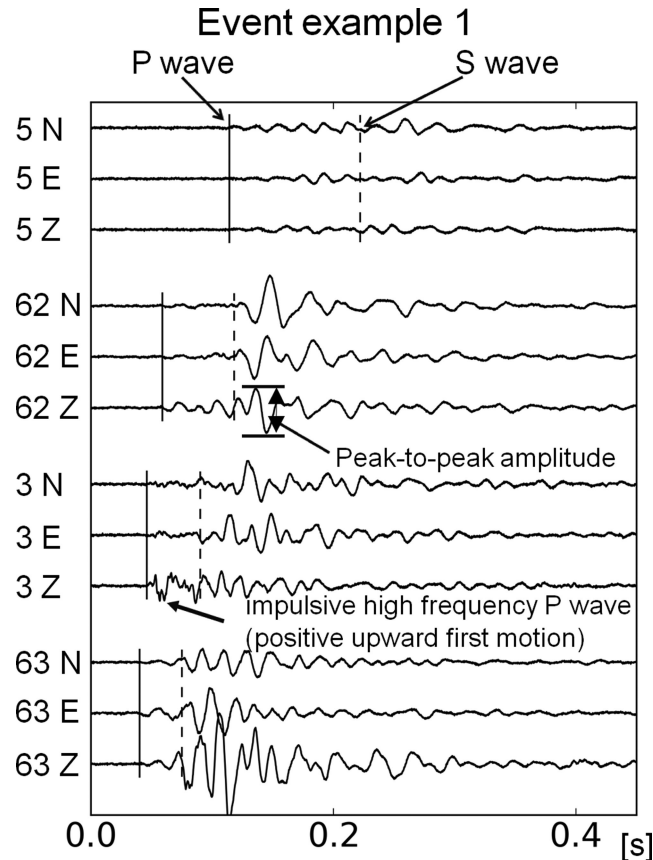
**Figure 4.** Microseismic wave form example. Unfiltered wave forms for event 1 (Fig. 3) shown for all four three-component stations.
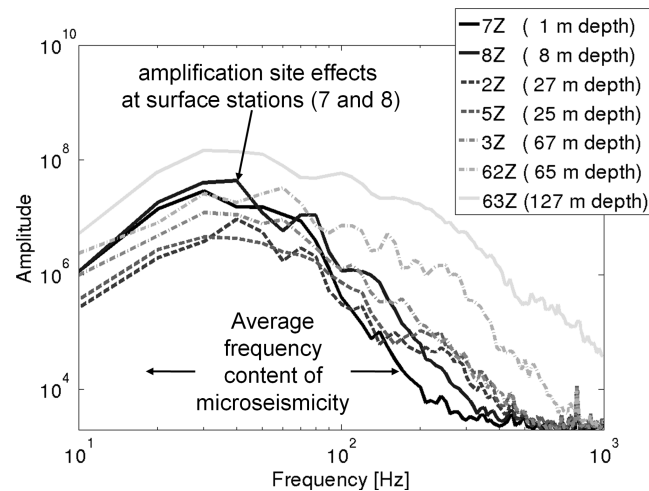


**Figure 5.** Spectral signal characteristics. Smoothed average spectra calculated for the Z component at each station for the 54 located events (Fig. 3). The average spectra are calculated over the frequency range of 10–1000 Hz, representing the mean spectral amplitudes for each 10 Hz interval.

velocity Dolomite layer (Fig. 6a), as well as a possible source effect associated with predominant upward *P*-wave radiation (Fig. 6b). It should be noted that the validation of these hypothesis is beyond the scope of this study and needs to be confirmed by detailed future study of source and propagation effects. Nonetheless, the observed wavefield characteristics have a significant impact on the design and functionality of the developed location approaches, and therefore, must be briefly discussed here.

The propagation effect on the wavefield is probably related to the seismic refraction of up going ray paths (Fig. 6a), due to the seismic velocity contrast between the stiff, high velocity Dolomite layer ($V_P \sim 5000$ m s$^{-1}$) and the less consolidated, slower over- and underlying Marl layers ($V_P \sim 3500$ m s$^{-1}$) associated with an expected critical angle of refraction around $\sim$44° (Table A1). Ray paths are principally refracted when travelling upward to stations 3 and 63 (Fig. 6a). Body wave traveltime residuals (*S–P* wave arrivals) at stations 3 and 63 are significantly smaller compared to those recorded at stations 5 and 62 (Fig. 6c), while their hypocentral distances remain similar. The
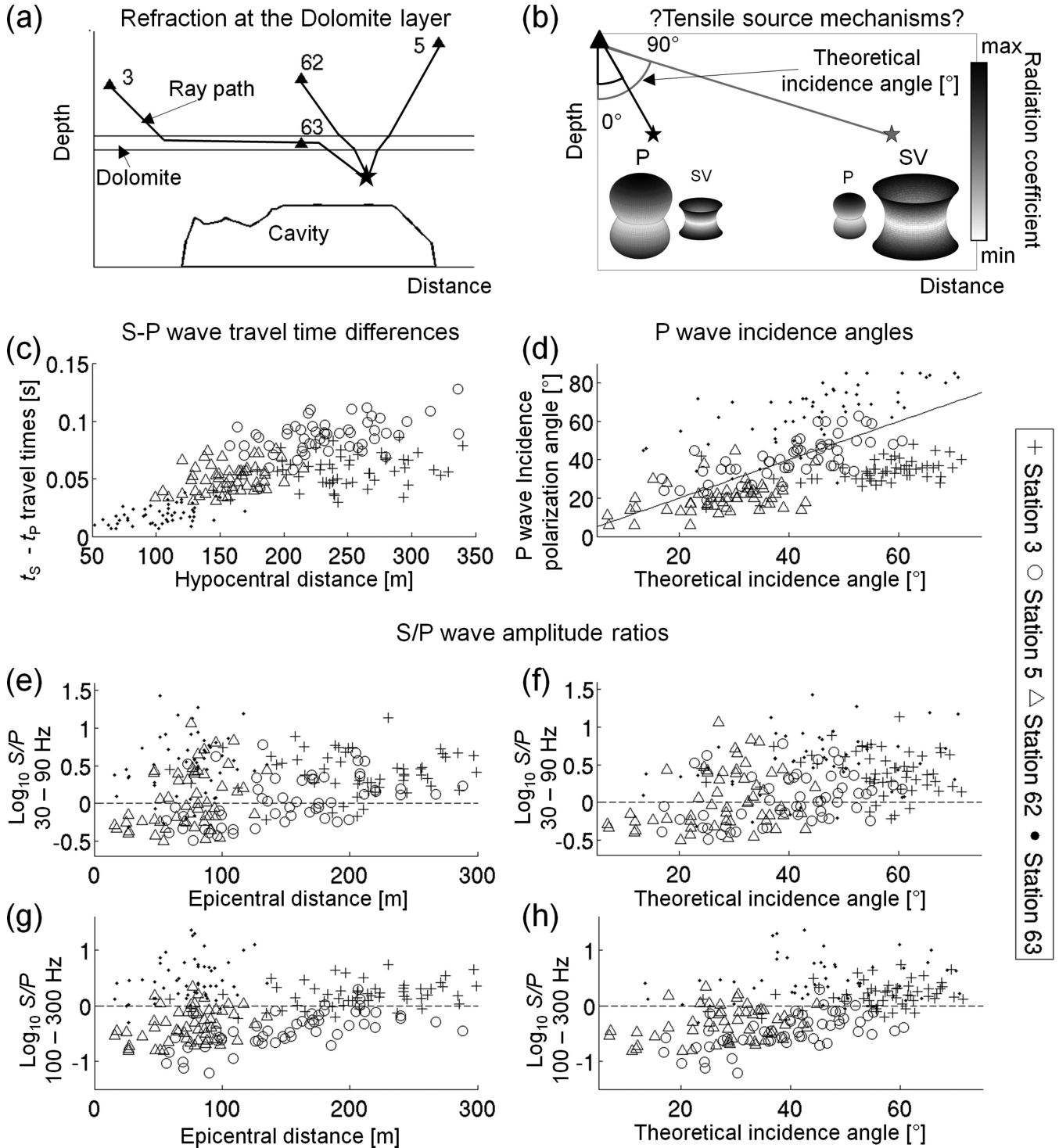
**Figure 6.** Propagation and source effects. Principal characteristics of the body wavefield with respect to the 54 located events (Fig. 3). Refracted ray paths along the Dolomite layer (a) are indicated by *S* minus *P*-wave traveltimes (c) and *P*-wave polarization angles (d) (Appendix). The predominance of tensile source mechanisms, associated with a maximal *P*-wave radiation coefficient vertically upwards and maximum *SV*-wave radiation coefficient at 45° (b), is indicated by the decrease in the *S/P* wave amplitude ratios at smaller epicentral distances and theoretical incidence angles at lower (e–f) and higher (g–h) frequencies (see text). The tensile source model and radiation pattern (view angle with vertical elevation of 20°) are taken from Kwiatek & Ben-Zion (2013) (provided by the matlab code available on http://www.mathworks.fr/matlabcentral/fileexchange/authors/201090). Question marks in the title indicate that the tensile source model fit by trend to the data however this hypothesis is speculative and need to be tested in future research. *S*- and *P*-wave amplitudes are estimated by the peak-to-peak phase amplitudes (Fig. 4) after station component rotation to an LQT (ray oriented) coordinate system (e.g. Plesinger *et al.* 1986).

smaller *S–P* time residuals result from longer wave propagation distances in the Dolomite layer associated with higher velocities and a smaller *Vp/Vs*–ratio as compared to the Marl layers (Table A1). Moreover, *P*-wave incidence polarization angles tend to be close to horizontal at station 63, and remain constant around the critical angle of refraction (30–45°) at station 3 (Fig. 6d, Appendix). At station 63, the observed wavefield is generally complicated and often not interpretable from ray theory, due to refraction at the Dolomite layer. One characteristic effect on wavefield amplitudes introduced by refraction at this station are strong amplitudes in the vertical component succeeding the *P*-wave arrival (Fig. 4), representing *P* and *SV* wave conversions close to station 63 as well as superimposed *P* and *SV* wave multiple reflections, and possibly inhomogeneous wave packets propagating with *S*-wave velocity. This hypothesis has been confirmed from observations on synthetic seismograms (not shown here) assuming a homogenous and layered velocity model in order to study the effects introduced by the Dolomite layer. Consistently, regarding the *S/P* ratio for higher frequencies (100–300 Hz) at station 63, a clear increase of the *S/P* ratio around the expected critical angle of refraction (30–50°) is observed which probably documents the presence of significant *P–SV* conversion at the Dolomite layer close to the station.

In addition to the presence of propagation effects, we shall consider source effects associated with dominant upward *P*-wave radiation as indicated by a slight increase of *S/P* peak-to-peak amplitude ratios with increasing epicentral distance and station incidence angle (Figs 6e–h). This systematic decrease might be for example explained by predominant tensile faulting with a vertical axis and dominant upward *P* wave and dominant *SV*-wave radiation at 45° (Fig. 6b) as commonly expected for the detachment of blocks at the cavity roof (e.g. Hasegawa *et al.* 1989). However, also pure dip-slip faulting can explain the dominant upward *P*-wave radiation. Consistently, from partial visual data inspection, we frequently observed clear positive upward first motion polarities of *P* wave for microseismic events located directly below the receiver (e.g. Fig. 4) which either might confirm the tensile source model or a dip-slip mechanisms associated with thrust faulting.

On the other hand, it cannot be excluded that the observed trends in the *S/P* ratios, especially when regarding lower frequencies, are affected by the presence of near-field effects. Given that the seismic wave velocities are in the order of 2400–3000 m s$^{-1}$ (Table A1), we obtain wavelengths of the order of 26–100 m for the lower frequencies (30–90 Hz) which is often in the same range as expected hypocentre distances (10–300 m). In addition, Mercerat *et al.* (2010) showed from standard spectral analysis (Brune 1970) that the source radius is in the order of one to several 10 m (6–31 m) for eight events recorded in 2005–2007. Assuming that these estimations are correct, it cannot be completely excluded that in some cases the estimated amplitudes are affected by near-field or directivity effects especially in cases of short source–receiver distance as it is generally the case for station 63. As a result, the interpretation of *S*- and *P*-wave amplitudes for lower frequencies (Fig. 6) for station 63 need to be considered with caution.

Nonetheless, the decrease of the *S/P* ratio can be consistently observed for lower (30–90 Hz) and higher frequencies (100–300 Hz), while *P* waves become more dominant compared to *S* waves when considering higher frequencies. The consistent decrease of the *S/P* ratio for both frequency bands generally supports the idea of a systematic source effect. On the other hand, the dominance of *P* waves for higher frequency can be explained by an abnormally strong attenuation behaviour for *S* waves or by a reduction of the low frequency *S/P* ratio by the presence of near-field effects. To prove either one of these hypothesis will be the object of future research (for some further discussion see Section 3.2.2).

## 3 METHODS

In this section, we present two combinable probabilistic location approaches which both take advantage of the *P* wave dominance in the wavefield at high frequencies (>100 Hz; Section 2.3). The first approach uses amplitude estimates and an attenuation law to obtain the hypocentre location (Section 3.1) following the principle of Battaglia & Aki (2003). The second approach is designed to identify significantly polarized, high frequency *P*-wave energies and their associated polarization angles at three-component stations (Section 3.2).

### 3.1 Location of microseismicity based on amplitude ratios

#### 3.1.1 Attenuation model

The influence of attenuation (Section 2.3) is assumed to follow a simple attenuation law (e.g. Battaglia & Aki 2003)

$$A\left(f\right) = s\left(f\right) \cdot A_0\left(f\right) \cdot \left({1}/{r^n}\right) \cdot \exp\left({\pi f r}/{Q V_P}\right), \tag{1}$$

describing the exponential amplitude decay with distance, where $A$, $A_0$, $s$ and $r$ are the corresponding signal amplitudes, the source amplitude, the receiver amplification site effect and the hypocentral distance, respectively. The coefficient $n$ represents the degree of amplitude loss due to geometric spreading, $V_P$ the medium's specific *P*-wave velocity, $f$ the considered frequency, $Q$ the Quality factor and exp the exponential function. In order to avoid any assumption about $A_0$, the attenuation law can be considered for amplitude ratios of a station couples with stations $i$ and $j$, as proposed by Taisne *et al.* (2011), that we then expressed in its logarithmic form

$$\log_{10}\left({A_i\left(f_k\right)}/{A_j\left(f_k\right)}\right) = \log_{10}\left({s_i\left(f_k\right)}/{s_j\left(f_k\right)}\right) + n\log_{10}\left({r_j}/{r_i}\right) - {\pi f_k}/{Q V_P}\left(r_i - r_j\right) \cdot \log_{10}(\exp 1), \tag{2}$$

where $f_k$, the frequency band.
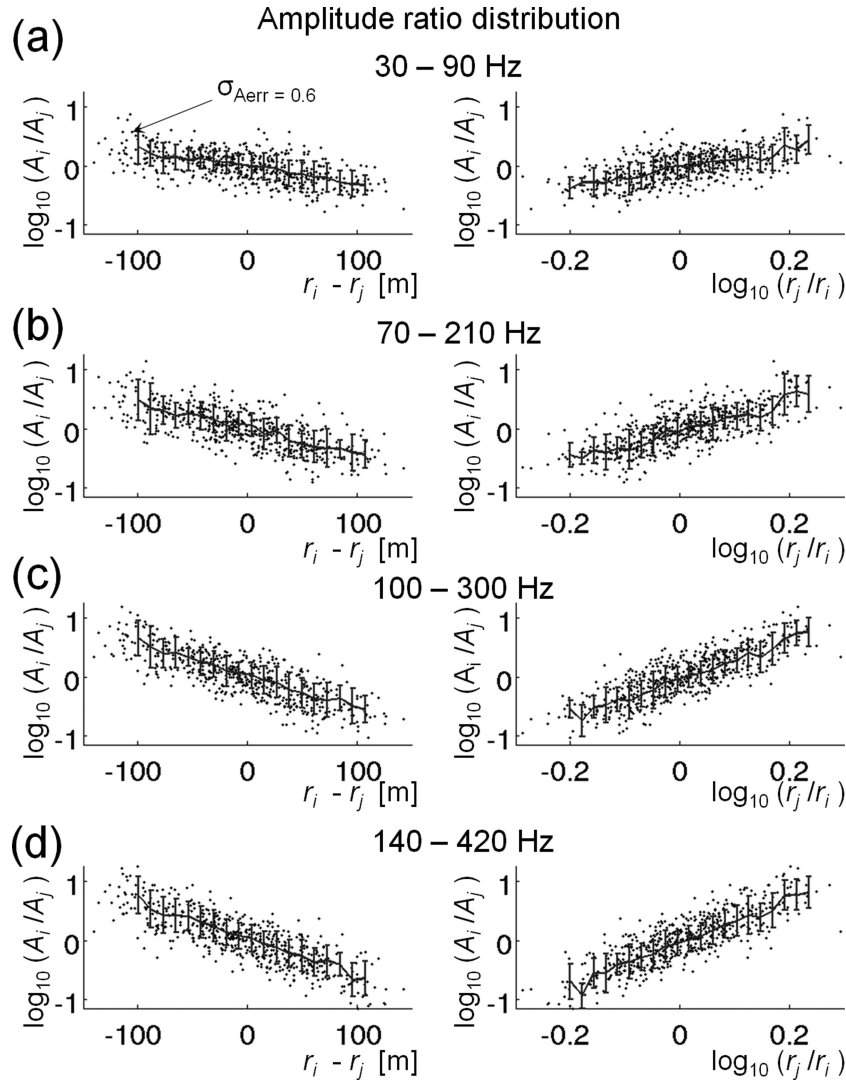
**Figure 7.** Effects of attenuation on amplitudes. Peak-to-peak amplitude ratio distributions versus distance terms described in eq. (2), with respect to all station couples and neglecting the stations at the cavity centre (6 1–3) (e.g. Fig. 1). Error bars indicate the measure of the uncertainty in the amplitude ratio determinations $\sigma_{Aerr}$ and represent the standard deviations related to a mean value (continuous black line) calculated at 30 points along the amplitude ratio distribution.

### 3.1.2 Amplitude calculation, correction and distribution

Signal amplitudes are determined by the peak-to-peak amplitudes on the vertical station components (Fig. 4) for four different frequency bands $f_k$ with increasing centre frequency: $f_1 = 30$–$90$ Hz, $f_2 = 70$–$210$ Hz, $f_3 = 100$–$300$ Hz and $f_4 = 140$–$420$ Hz. The rms amplitude approximation is less appropriate to determine signal energy from the observed microseismic data as it depends on the chosen time window for a seismic event. Regarding the complicated and strongly varying phase signature of tremor-like swarming sequences (Fig. 2), as presented in Section 2, an accurate determination of the starting and end time of a seismic event is generally difficult.

Using the 54 isolated events of well-constrained hypocentre locations (Fig. 3), the ratio of amplification site effects with respect to one station couple was determined by using the amplitude ratios for those events that are located at very similar hypocentral distance ($\pm 20$ m) with respect to both stations. If both station-hypocentre distances are of same order, the attenuation effects can be neglected and the observed amplitude ratios represent a first approximation of the ratio of amplification site effects (eq. 2). In this way, the amplification site effect ratio was determined with respect to each station pair by using the mean of the amplitude ratios of the selected events.

Even though this correction for amplification site effects as well as the assumed attenuation law do not account for 3-D attenuation effects introduced by the cavity zone (e.g. Fig. 4), the final amplification corrected amplitude ratios for the 54 events show a clear functional relationship with the distance-depending terms of eq. (2) (Fig. 7). As a result, the amplitude decay with distance is smooth, and the 1-D attenuation law seems to be an appropriate choice to model the observed attenuation effects (Section 2.3) without accounting for 3-D attenuation effects. At higher frequencies, variations of amplitude ratios become significantly larger compared to lower frequencies, which agrees with the observed increase of attenuation effects at frequencies of $\geq 100$ Hz (Figs 5 and 7, Section 2.3).

### 3.1.3 Calibration of the attenuation law (probabilistic forward model)

The 54 located events were used to calibrate the attenuation law represented by the parameters $n$ and $Q$ (Fig. 3, eq. 2). We used a probabilistic formulation for the parameter search of $n$ and $Q$, represented by the posterior probability density $\sigma$ as denoted by Tarantola (2005), and Tarantola & Valette (1982)

$$\sigma(Q, n) = \kappa \cdot \rho_M(Q, n) \rho_D[g(Q, n)], \tag{3}$$

where $\rho_M$ is the prior probability density in the model space $M$, $\rho_D$ the probability density for $Q$ and $n$ represented by the information of the observed amplitude ratios, $\kappa$ the normalization constant and $g$ the functional relationship $\mathbf{d} = \mathbf{g(m)}$ between the elements $\mathbf{m} \in M$ of the model space and $\mathbf{d} \in D$ of the data space $D$ given by eq. (2). It is assumed that the uncertainties in the forward simulation of eq. (2) are generally negligible compared to the errors in the observed amplitude ratios and expected hypocentre locations (Fig. 3, Appendix). In the attenuation model, $V_P$ is valued as the expected minimum mean velocity of 2900 m s$^{-1}$ (Mercerat *et al.* 2010, Appendix, Table A1). Furthermore, $\rho_M$ is considered to be uniform with equal *a priori* probabilities within the intervals of the Cartesian product $\mathbf{Q} \times \mathbf{n}$ of the parameter sets $\mathbf{n} = \{0.3, 0.4, \ldots, 2.9, 3.0\}$ and $\mathbf{Q} = \{1, 2, 3, \ldots, 299, 300\}$. Model space sampling is based on a grid search where the probability density $\rho_D$ is defined as the exponential distribution of absolute differences ($L1$-norm) of the observed and calculated amplitude ratios $A$, so that it follows

$$\sigma(f_k; \mathbf{Q} \times \mathbf{n}) = \kappa \exp\left\{-\sum_j \sum_i \frac{\left|A^i_{\text{obs}}(f_k, x_j, y_j, z_j) - A^i_{\text{calc}}(f_k, x_j, y_j, z_j; \mathbf{Q} \times \mathbf{n})\right|}{\sigma_{\text{Aerr}}}\right\}, \tag{4}$$

where $i$ is the number of observed amplitude ratios for all station couples with respect to an event $j$ from the 54 located events with coordinates $x, y, z$ (Fig. 3), and $\sigma_{\text{Aerr}}$ represents the uncertainties in the observed amplitude ratios, the assumed attenuation model, and the hypocentral location errors (Appendix). The value for $\sigma_{\text{Aerr}}$ was estimated at $\pm 0.6$, corresponding to the maximum observed amount of scattering in the amplitude ratios (maximal standard deviation), relative to the receiver distance ratios and differences (Fig. 7).

The shapes of the probability density functions (PDF) indicate a trade-off between parameters $n(f_k)$ and $Q(f_k)$ for each frequency band $f_k$ (Fig. 8a). As a result, the stated inverse problem (eq. 2) is severely ill-posed with respect to the assumed attenuation model. In order to resolve this trade-off we assumed that the parameter $n$ (geometric spreading) is frequency-independent, as predicted by the attenuation model. As a result, we calculated the marginal PDF for $n$ with respect to all frequency bands $f_k$ by

$$\sigma_n(\mathbf{Q} \times \mathbf{n}) = \int_Q \sigma(f_1; \mathbf{Q} \times \mathbf{n}) \partial \mathbf{Q} \cdot \int_Q \sigma(f_2; \mathbf{Q} \times \mathbf{n}) \partial \mathbf{Q} \cdot \int_Q \sigma(f_3; \mathbf{Q} \times \mathbf{n}) \partial \mathbf{Q} \cdot \int_Q \sigma(f_4; \mathbf{Q} \times \mathbf{n}) \partial \mathbf{Q} \tag{5}$$

which is shown in Fig. 8(b) with a maximum likelihood at $n = 1.7$. The increased value of the coefficient of geometric spreading, departing from $n = 1$ for a spherically expanding body wave, might result from complexities in the wave front introduced by refraction at the Dolomite layer (Fig. 6). In the case of refracting wavefields, increased values for $n$ have been already reported from theoretical studies that showed that $n = 2$ for critically refracted $P$ waves (head waves) (Aki & Richards 2002) and $n = 1.5$ for direct $P$ waves emitted from sources located below a refractor (Campillo *et al.* 1984). Also regional empirical studies reported increased geometric spreading coefficients $n = 1.77$ estimated from Moho head waves $Pn$ (Zhu *et al.* 1991). Nonetheless, quantitative modelling of the effects of geometric spreading of the Dolomite layer is beyond the scope of the present paper.

The marginal probability for $n$ as representative for all frequency bands was then used in order to determine the marginal probabilities for $Q(f_k)$ at each frequency band $f_k$ by

$$\sigma_Q(f_1; \mathbf{Q} \times \mathbf{n}) = \int_n \sigma(f_1; \mathbf{Q} \times \mathbf{n}) \cdot \sigma_n(f_{2-4}; \mathbf{Q} \times \mathbf{n}) \cdot \partial \mathbf{n}$$

$$\sigma_Q(f_2; \mathbf{Q} \times \mathbf{n}) = \int_n \sigma(f_2; \mathbf{Q} \times \mathbf{n}) \cdot \sigma_n(f_{1,3-4}; \mathbf{Q} \times \mathbf{n}) \cdot \partial \mathbf{n}$$

$$\sigma_Q(f_3; \mathbf{Q} \times \mathbf{n}) = \int_n \sigma(f_3; \mathbf{Q} \times \mathbf{n}) \cdot \sigma_n(f_{1-2,4}; \mathbf{Q} \times \mathbf{n}) \cdot \partial \mathbf{n} \tag{6}$$

$$\sigma_Q(f_4; \mathbf{Q} \times \mathbf{n}) = \int_n \sigma(f_4; \mathbf{Q} \times \mathbf{n}) \cdot \sigma_n(f_{1-3}; \mathbf{Q} \times \mathbf{n}) \cdot \partial \mathbf{n}$$

The marginal probabilities for $Q(f_k)$ at each frequency band are shown in Fig. 8(b). The obtained maximum likelihoods indicate a slight dependence of $Q$ with frequency. $Q$ factors are generally found in the range of 40–60, which generally agrees with the results obtained by Mercerat (2007), and Mercerat *et al.* (2010), who found $Q = 10–30$ for $P$ waves at frequencies $<100$ Hz using a spectral amplitude ratio method. Since, at higher frequencies, $P$ waves dominate the seismic signals more than $S$ waves (Fig. 6), the $Q$ factors refer to the attenuation behaviour of $P$ waves (Fig. 8b). On the other hand, Mercerat *et al.* (2010) showed that $Q$ factors for $S$ and $P$ waves are of the same order of magnitude.

The uncertainties in $Q$'s maximum likelihoods decrease at increasing frequencies, shown by the bell-shaped PDF curves that clearly become less dispersive and have more symmetric geometries. This observation might indicate that intrinsic attenuation dominates at higher frequencies. For lower frequencies, between 30 and 90 Hz, the maximum likelihood for $Q$ converged to infinity, indicating that attenuation is predominantly contributed by geometric spreading, while intrinsic attenuation is negligible (Fig. 8b). The predominance of geometric
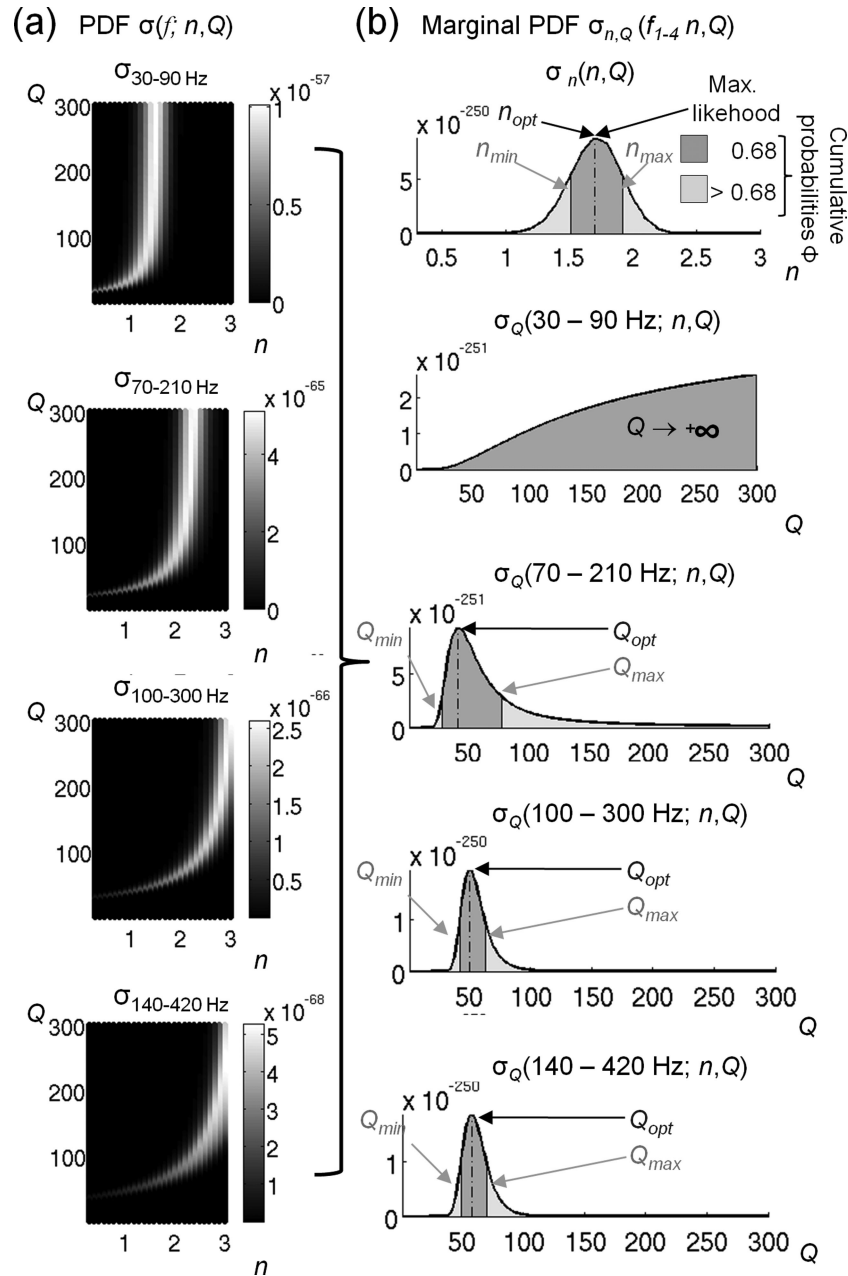
**Figure 8.** Probabilistic estimates of $n$ and $Q$. Parameter estimation for $n$ and $Q$; (a) PDFs with respect to parameters $n$ and $Q$ are calculated for four frequency bands using eq. (4). (b) Marginal PDFs for $n$ calculated from eq. (5) (upper panel), and for $Q$ with respect to all frequency bands as calculated from eq. (6) (panels below) (see text). Named indices (*min*, *opt*, *max*) for $n$ and $Q$ correspond to the parameters values (Table 1) which represent the region (dark grey shaded area) of the maximum likelihood (*opt*) (dashed line) and those located next to it (*min* and *max*) (light grey shaded areas) defined by the cumulative probability equal to 0.68 (see text).

spreading at lower frequencies and predominance of intrinsic attenuation at higher frequencies is quite reasonable, considering eq. (2). For lower frequencies, hypocentral distances and wavelengths are of the same order of magnitude such that the magnitude of intrinsic attenuation becomes comparatively small.

For our attenuation estimations, and in the following location approach, stations 62 and 63, located at the centre of the cavity, were not considered, because amplitudes observed at both stations are more sensitive to absolute source depths compared to stations located along the cavity border. Source depth estimations by our classical location approach for the 54 events are based on significant uncertainties (Appendix) which might introduce a bias in our results when including stations 62 and 63. Furthermore, in the case of station 63, the wavefield observed on its vertical component is complicated and not dominated by *P* waves, as it is the case for the other stations, but comprises multiple *P–SV* conversions or inhomogeneous waves (Fig. 4, Section 2.3).

**Table 1.** Three $n$ and $Q$ values, and their corresponding weights are shown for each frequency band, related to the region of the maximum likelihood locations and those next to it (Fig. 8b, Section 3.1.3).

| Frequency | $n_{min}$ | Weight $n_{min}$ | $n_{opt}$ | Weight $n_{opt}$ | $n_{max}$ | Weight $n_{max}$ | $Q_{min}$ | Weight $Q_{min}$ | $Q_{opt}$ | Weight $Q_{opt}$ | $Q_{max}$ | Weight $Q_{max}$ |
|---|---|---|---|---|---|---|---|---|---|---|---|---|
| 30–90 Hz | 1.51 | 0.17 | 1.7 | 0.67 | 1.92 | 0.16 | | | | | | |
| 70–210 Hz | 1.51 | 0.085 | 1.7 | 0.335 | 1.92 | 0.08 | 28 | 0.025 | 41 | 0.325 | 78 | 0.15 |
| 100–300 Hz | 1.51 | 0.085 | 1.7 | 0.335 | 1.92 | 0.08 | 42 | 0.04 | 50 | 0.335 | 63 | 0.125 |
| 140–420 Hz | 1.51 | 0.085 | 1.7 | 0.335 | 1.92 | 0.08 | 49 | 0.05 | 58 | 0.34 | 70 | 0.11 |

### 3.1.4 Probabilistic location based on amplitudes

The calibrated attenuation law, based on parameters $n$ and $Q$, can now be used to calculate the theoretical amplitude ratios which we will then compare with the observed ratios, in order to determine the hypocentre locations. We formulated this location procedure in a probabilistic manner with consideration for uncertainties in $n$ and $Q$.

The probabilistic solution used (Tarantola & Valette 1982; Tarantola 2005) is given by

$$\sigma(\mathbf{X}, \mathbf{Y}, \mathbf{Z}) = \kappa \cdot \rho_M(\mathbf{X}, \mathbf{Y}, \mathbf{Z}) \, \rho_D [g(\mathbf{X}, \mathbf{Y}, \mathbf{Z})], \tag{7}$$

where $\mathbf{X}, \mathbf{Y}, \mathbf{Z}$ represent the Cartesian coordinates of the potential source location. The coordinate system was restricted to the cavity region (e.g. Fig. 1), assuming equal *a priori* probabilities to equal volumes, defined by a 10 m grid as represented by the Cartesian product $\times$ of the sets X = {220, . . . , 590}, Y = {40, . . . , 450} and Z = {−250, . . . , −60}. For simplification, the uncertainties to be given to the parameters $n$ and $Q$ were not the continuous marginal PDFs, but were extracted from the PDFs as three possible values for each parameter, defined as the 'min', 'opt' and 'max' values of the respective PDF shown in Fig. 8(b). These values are calculated from the PDFs so that the 'opt' corresponds to the maximum likelihood, and the 'min' and 'max' brackets the 0.68 probability level. For the three highest frequency ranges, both $Q$ and $n$ are thus represented by $m = 3$ possible values, each of them having a specific weight (see Table 1), leading to $m = 9$ possible combinations; for the lowest frequency range, Q is not defined, so that only $m = 3$ possible cases arise (values of $n$).

Thus, for inversion, a set of $m = 9$ entries $\mathbf{E}(f_k) = \{(n_1, Q(f_k)_1), (n_2, Q(f_k)_2), \ldots, (n_m, Q(f_k)_m)\}$, represent all possible combinations of the three parameter values for $n$ and $Q$ obtained for each frequency band, except for the frequency band of 30–90 Hz for which $m = 3$. Each entry of $\mathbf{E}(f_k)$ is associated with a weight $w(f_k)_m = \Phi\left(\mathbf{E}(f_k)_m\right)/\Phi\left(\mathbf{E}(f_k)\right)$ corresponding to the cumulative probabilities $\Phi$ found for each parameter combination (Table 1). Then the *posterior* probability density for one frequency band $f_k$ and one seismic event is obtained by the weighted product of independent probability densities calculated for each parameter combination and the *L1* distances between the observed and calculated amplitude ratios $A$ for a station couple $i$

$$\sigma(f_k\mathbf{X}, \mathbf{Y}, \mathbf{Z}) = \prod_i \left[ \frac{1}{m} \sum_m w(f_k)_m \cdot \kappa \exp\left\{ -\frac{\left| A^i_{obs} - A^i_{cal}\left(\mathbf{E}(f_k)_m; \mathbf{X}, \mathbf{Y}, \mathbf{Z}\right)\right|}{\sigma_{Aerr}} \right\} \right]. \tag{8}$$

The final *posterior* probability density of hypocentre location $\sigma_{amp}$ is then found by the conjunction of the probability densities for all frequency bands

$$\sigma_{amp}(\mathbf{X}, \mathbf{Y}, \mathbf{Z}) = \frac{1}{\nu} \prod_k \sigma(f_k\mathbf{m}; \mathbf{X}, \mathbf{Y}, \mathbf{Z}), \tag{9}$$

where $\nu$ is a normalization constant (Tarantola & Valette 1982; Tarantola 2005).

## 3.2 Hypocentre determinations from high frequency polarized *P*-wave energies

### 3.2.1 Estimating the degree of linearly polarized energies

The following method was developed in order to identify automatically *P*-wave phases and their associated polarization angles for three-component stations. Different from conventional polarization analyses that use eigenanalysis of particle motion (e.g. Flinn 1965), our approach instead uses simple peak-to-peak amplitudes estimates to determine the degree of linearly polarized energy in the signal, and hence, it is a more robust method with respect to the choice in the length of the window of analysis and the considered wave periods.

For a time window $t$, the maximum polarized energy $L$, associated with a specific receiver backazimuth $\varphi$ and an incidence angle $\theta$, is approximated as the maximum of the ratio (logarithmic subtraction)

$$L_{t,\varphi,\theta} = \underset{\varphi \times \theta}{\operatorname{argmax}}\left\{ \log_{10}\left(l_t(\varphi \times \theta)\right) - \frac{1}{2}\left[\log_{10}\left(q_t(\varphi \times \theta)\right) + \log_{10}\left(t_t(\varphi \times \theta)\right)\right] \right\}, \tag{10}$$

where $l$, $q$, and $t$ (please do not confuse with $t$) represent the peak-to-peak amplitudes estimated from each axis of the LQT (ray oriented) coordinate system (e.g. Plesinger *et al.* 1986). The axes of the LQT system and the respective $l$, $q$, $t$ amplitudes are explored with respect to all directions of the half space below the considered receiver (Fig. 9). The directions are discretized by direction vectors defined by the Cartesian product $\times$ of a set of potential backazimuths $\varphi = \{0°, 10°, \ldots, 340°, 350°\}$ and incidence angles $\theta = \{0°, 10°, \ldots, 80°, 90°\}$. Consequently, we assume that the seismic energy always originates from below the receiver, resolving the $\pm180°$ ambiguity for the backazimuth angle. The resulting $L$-value can be seen as a measure of the degree of linearly polarized energy.
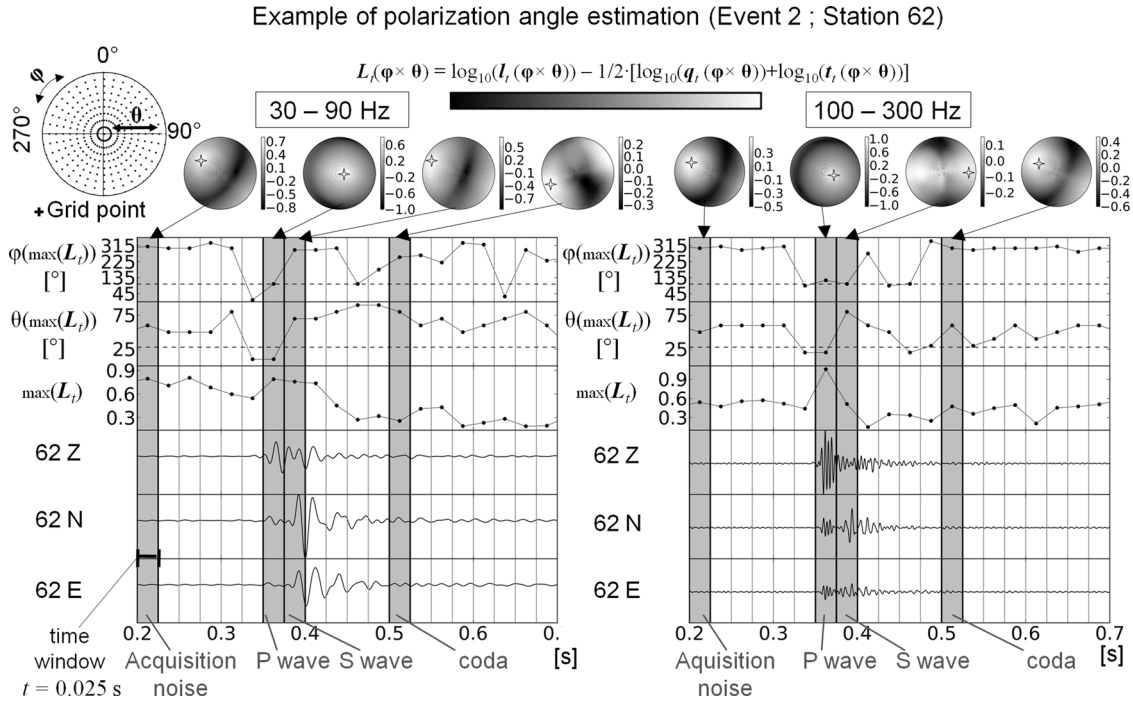
**Figure 9.** Example of *P*-wave analysis. Demonstration of *P* wave phase identification and polarization angles at station 62 for event 2 (Fig. 3) for the frequency bands of 30–90 Hz (lower left-hand panel) and 100–300 Hz (lower right-hand panels) using the *L*-value method (eq. 10, Section 3.2.1). *L*-values were calculated for 0.025 s time windows (grey and black vertical lines) corresponding to a backazimuth $\varphi$ and incidence angle $\theta$. Dashed lines mark the actual backazimuth and incidence angles with respect to event 2 (Fig. 3). *L*-value calculation is illustrated (upper hemisphere plot) for four windows (grey shaded areas) showing the maximal *L*-value (star in hemisphere plot) corresponding to acquisition noise, *P* and *S* waves and coda portions.

### 3.2.2  *P*-wave phase identification

As discussed in Section 2.3 and shown by the *S*/*P* amplitude ratios in Fig. 6, *P*-wave energies become dominant in the body wavefield when considering higher frequencies (>100 Hz), small hypocentral distances and steeper incidence angles. Fig. 9 shows the ability of the *L*-value method to successfully identify such cases of dominating *P*-wave energies at higher frequencies, with respect to event 2 (Fig. 3). At higher frequencies, the degree of polarization for *S* waves (*L*-value = 0.6) is significantly lower compared to *P* waves (*L*-value = 1.1), while at lower frequencies the degree of polarization is in the same order of magnitude for *P* and *S* waves (*L*-value = 0.7; Fig. 9). Furthermore, the degree of linear polarization with respect to the acquisition noise is weaker at higher frequencies (*L*-value = 0.5) compared to lower frequencies (*L*-value = 0.8), so that the *P*-wave contribution in the seismogram is represented by significantly higher *L*-values, relative to noise.

The capability of the *L*-value method to automatically identify significantly polarized high frequency *P*-wave energy portions is demonstrated in Fig. 10(a). This method was applied to the seismograms of the 54 located events (including noise, seismic events and codas) (Fig. 3) for the three-component stations 3, 5 and 62, at a high (100–300 Hz) and a low (30–90 Hz) frequency band, using a time window *t* of length 0.025 s. Station 63 is completely neglected in this approach because arrival time residuals between *P* and *S* waves are very short (<0.01 s, Fig. 6c) with respect to the time window length used and, because ray theory often becomes invalid due to refraction at the Dolomite layer (Figs 4 and 6, Section 2.3).
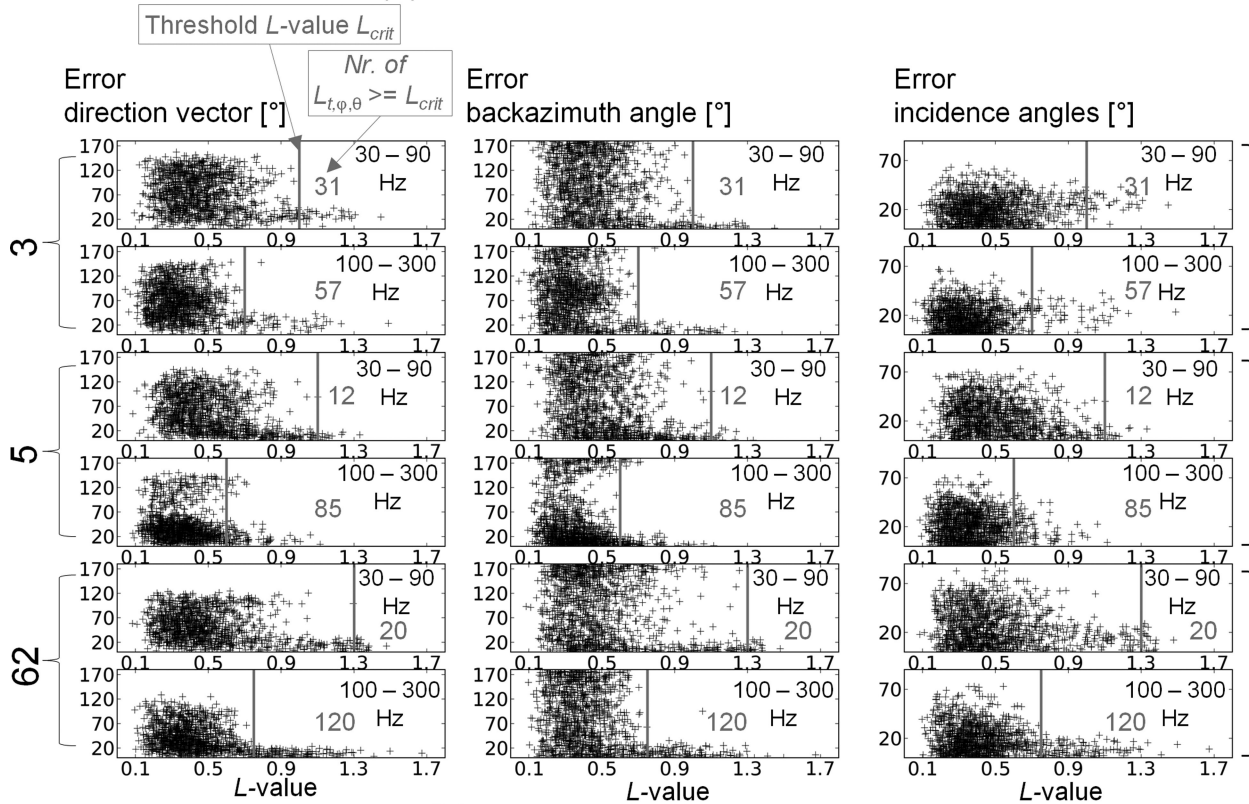
In Fig. 10(a), the errors of the estimated direction vectors and the related backazimuth and incidence angles are shown as a function of the corresponding *L*-values (degree of polarization). The errors in the polarization angles are represented by the differences between the estimated and the calculated direction vectors and of their related backazimuth and incidence angles, assuming a homogeneous velocity model (for further explanations see Section 3.2.3).

Regarding the *L*-values and the corresponding errors in the polarization angles, it can be observed that for a specific *L*-value (degree of polarization) the errors in the polarization angles remain significantly small compared to errors associated with lower *L*-values. For each station and frequency band, this specific *L*-value is defined as the threshold value $L_{\text{crit}}$. In the following, this threshold value is used for the detection of significantly polarized *P*-wave energies within the considered time windows.

The quantity of *L*-values $\geq L_{\text{crit}}$ is much larger at higher frequencies than at lower frequencies (Fig. 10a), in agreement with the principal observation that *P* waves are more dominant than *S* waves at higher frequencies (Figs 6 and 9, Section 2.3). The increasing degree of polarization with higher frequencies might be also explained by the fact that the observed wavelengths become smaller, and therefore, the wavefield is better approximated by assumed ray theory (high frequency approximation). In addition, most polarized *P*-wave energies can be detected at station 62, using the defined threshold of $L_{\text{crit}} = 0.75$ (Fig. 10a), consistent with the observation that *P* waves become increasingly dominant at smaller hypocentral distances and steeper incidence angles (Figs 6 and 10a).
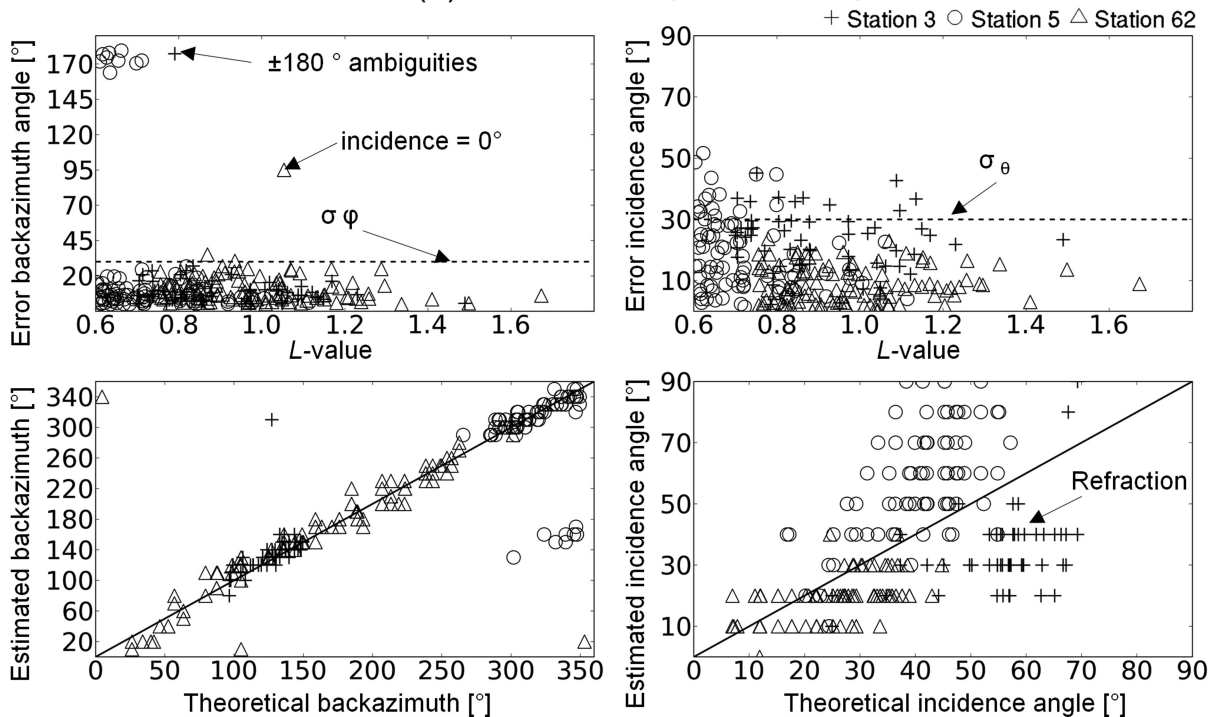
**Figure 10.** Distribution of linearity and polarization angles. (a) Errors in the estimated direction vectors (left-hand panels), the related backazimuths (middle panels) and incidence angles (right-hand panels), as a function of the corresponding $L$-values (black points) calculated for 0.025 s time windows for all seismograms of the 54 located events (Fig. 3) and for three-component stations 3, 5 and 62, at frequency bands of 30–90 Hz and 100–300 Hz (see text). Errors in polarization angles were calculated by the absolute deviation of the estimated polarization angles with respect to the expected backazimuth and incidence angle found from the location of the 54 events. $L$-values greater than the thresholds (grey lines) $L_{crit}$ indicate significantly polarized $P$-wave energies. (b) Quality and errors of the determined polarization angles associated with $L$-values $\geq L_{crit}$ for the 100–300 Hz frequency band. Theoretical incidence angles correspond to the angles pointing towards the source at 0° and 90° in vertical and horizontal directions, respectively, with regards to the station (Fig. 6b).

The lowest amount of *L*-values beyond the threshold $L_{crit}$ is observed at station 3 (Fig. 10a), which is logical, since the *S* waves dominate for larger theoretical incidence angles as shown in Fig. 6. Accordingly, a noticeable cluster of polarized *SH*-wave energies is observed at higher frequencies and *L*-values below the threshold value ($L_{crit} = 0.7$) associated with an indicative error of ∼90° in the backazimuth angle (Fig. 10a). This observation can be explained by a dip-slip faulting mechanism for which the *SH–SV* amplitude ratio increase at increasing ray incidence (while also dependent on the ray azimuth), as a result of radiation pattern expected when assuming a standard dip-slip shear dislocation model (double-couple force model). In addition, the absence of a distinct *SH*-wave cluster at lower frequency might generally confirm our hypothesis that ray theory is better approximated when regarding higher frequencies.

However, even though the theoretical average incidence angles at station 5 are expected to be not dramatically smaller compared to station 3, no comparable *SH*-wave energy cluster can be observed for higher frequencies. This lack of *SH*-wave energies at higher frequency might be related to abnormal high *S*-wave attenuation behaviour as suggested from the significant decrease in the *S/P* ratios at increasing frequencies which is most significant for station 5 (Figs 6e–f). We suggest that this particular high *S*-wave attenuation at station 5, which is located at shallower depth than stations 3, 62 (∼35 m) and 63 (∼102 m), could be principally related to a fractured and unconsolidated state of the overburden and partial saturation in the pore spaces of ground water. Consistently, in a seismic tomography campaign, Kosecki *et al.* (2010) documented very low *P*-wave velocities for the uppermost sedimentary layers (<50 m depth) of around 1.7 km s$^{-1}$. These velocities suggest a clearly water saturated state what is consistent with water level measurements in the exploitation wells by SOLVAY, documenting ground water levels at approximately 30 m depth.

Despite the fact that the origin of the absence of high frequency *S*-wave energy at station 5 cannot be completely resolved by this study, the resulting predominance of *P*-wave energies has a positive feedback to the detection capability by using our *P* wave based polarization approach. Consequently, the critical *P*-wave detection value at station 5 could be defined for a relatively low level, $L_{crit} = 0.6$, compared to the other stations.

On the other hand, the estimated polarization angles are partially erroneous with ±180° ambiguities in the backazimuth angles and overestimated incidence angles (Fig. 10a). Since station 5 is located at shallower depth, these errors might be related to secondary *P*-wave phases reflected at the free surface which, when contained in the particle motion, lead to misestimations of the true incidence angles (e.g. Neuberg & Pointer 2000).

### 3.2.3 *Probabilistic location based on polarization angles*

In this section, we explain how we use the identified *P*-wave polarization angles (Fig. 10a, Section 3.2.2) to constrain hypocentre locations. We chose a probabilistic approach in order to render location results comparable with the amplitude-based approach (Section 3.1), and to account for the varying detectability and quality of the *P* phases and their polarization angles, at each station (Fig. 10, Section 3.2.2).

*P*-wave phase and polarization angle determination is generally performed using the high frequency band because comparatively more *P* waves phase can be identified (Figs 9 and 10). For several cases amongst the 54 considered events, more than one *P*-wave phase and polarization angle was identified (Fig. 10a). For station 62, the total number of determined polarization angles (120) is more than twice the total of events considered (54). On the other hand, polarization angles for certain events could not be identified for all stations. It should be noted that not all of the identified *P* phases are related to the 54 events. Similar to the isolated event swarming sequences in Fig. 2, the seismograms of the 54 events are accompanied by small precursor and multiplet events appearing before and after the main seismic event.

In order to relate the identified polarization angles determined at each station to the same seismic event, all the corresponding time windows per station $\boldsymbol{t}^{stat.} = \{t_1, t_2, \ldots, t_n\}$ are combined to a set representing the potential source origin times $T_0^{stat.}$.

$$\boldsymbol{T}_0^{stat.} = \boldsymbol{t}^{stat.} - \frac{\boldsymbol{R}^{stat.}}{V_P}, \tag{11}$$

where $\boldsymbol{R}^{stat.}$ represents the distances between the station and the **X**, **Y**, **Z** gridpoints, defined in Section 3.1.4. Then, the sets of source origin times for all stations are united to one set $\boldsymbol{T}_0$ representing all potential source time origins

$$\boldsymbol{T}_0 = \boldsymbol{T}_0^3 \cup \boldsymbol{T}_0^5 \cup \boldsymbol{T}_0^{62}, \tag{12}$$

where ∪ marks the set's theoretic union. In the final step, the source origin times for one event are represented by a time $\tau$ defined from the spacing intervals of the time samples $T_i$ in $\boldsymbol{T}_0$ from the conditional functional relationship

$$\tau_{start-end} = \begin{cases} \text{if } i = 0 \vee T_i - T_{i-1} \geq 0.05 & \text{then } \tau_{start} = T_i \\ \text{if } T_i - T_{i+1} \leq -0.05 & \text{then } \tau_{end} = T_i \end{cases}, \tag{13}$$

where ∨ denotes the logical disjunction (or). In other words, a new event associated with the source origin times $\tau$ is identified in the set $\boldsymbol{T}_0$ when the difference between two adjoined time samples exceeds 0.05 s corresponding to double the length of the chosen time window $t$ (0.025 s) used for the *L*-value method (Section 3.2.2).
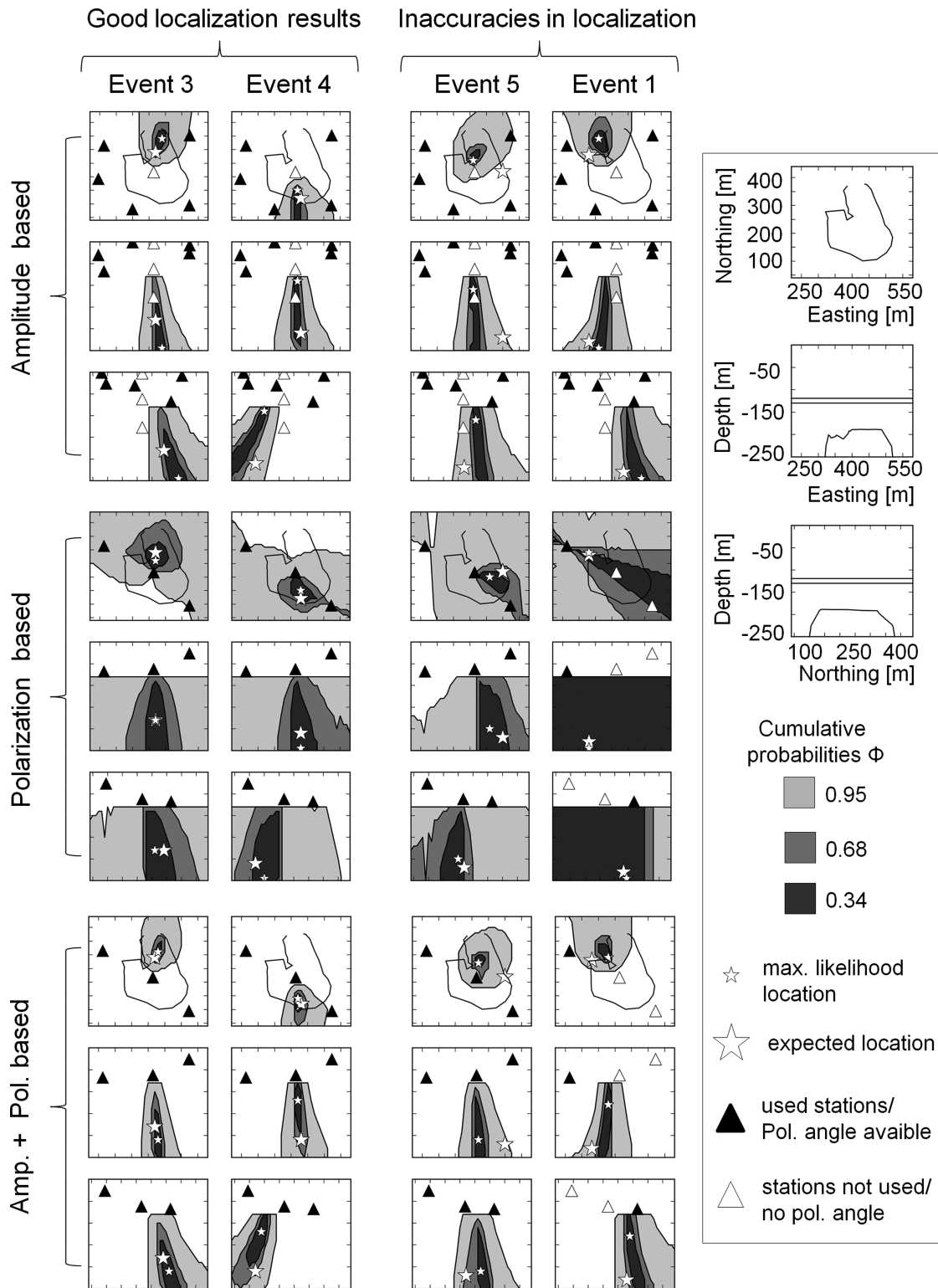
**Figure 11.** Probability density functions for location. Cumulative probabilities (Φ) with contours equal to 0.34, 0.68 and 0.95, and the maximum likelihood locations (small stars), for two good (left-hand panels) and two problematic (right-hand panels) location results using the amplitude-based (upper panels), the polarization-based (middle panels), and the combination of the latter two (lower panels) in comparison with the expected hypocentre location (big star) estimated from the classical location approach for the 54 events.

For every seismic event associated with the time interval $\tau$, the *posterior* probability density of the hypocentre location is then expressed by the L2 misfit between m observed and calculated backazimuth $\varphi$ and incidence $\theta$ angles obtained for one station with uncertainties $\sigma_\varphi$ and $\sigma_\theta$

$$\sigma_{\text{stat.}}(\mathbf{X}, \mathbf{Y}, \mathbf{Z}, \tau) = \frac{1}{m} \sum_k^m \kappa \exp\left(-\frac{\left(\varphi_{\text{obs}}^k - \varphi_{\text{calc}}(\mathbf{X}, \mathbf{Y}, \mathbf{Z}, \tau)\right)^2}{2\sigma_\varphi^2} - \frac{\left(\theta_{\text{obs}}^k - \theta_{\text{calc}}(\mathbf{X}, \mathbf{Y}, \mathbf{Z}, \tau)\right)^2}{2\sigma_\theta^2}\right). \tag{14}$$

The index $k$ refers to those polarization angles whose time window $t^{\text{stat}}$ satisfies the condition

$$\tau \cap t^{\text{stat.}} - \frac{\mathbf{R}^{\text{stat.}}}{V_P} \neq \emptyset, \tag{15}$$

where Ø denotes an empty set. In other words, we choose those polarization angles whose set of potential source origin times is compatible with the event time $\tau$. Finally, the conjunction of probability densities for all stations gives the *posterior* probability density $\sigma_{\text{pol}}$ for one event location

$$\sigma_{\text{pol}}(\mathbf{X}, \mathbf{Y}, \mathbf{Z}, \tau) = \sigma_3(\mathbf{X}, \mathbf{Y}, \mathbf{Z}, \tau) \cdot \sigma_5(\mathbf{X}, \mathbf{Y}, \mathbf{Z}, \tau) \cdot \sigma_{62}(\mathbf{X}, \mathbf{Y}, \mathbf{Z}, \tau). \tag{16}$$

The parameter setting chosen for the practical implementation of this probabilistic location scheme is summarized in Fig. 10(b), which illustrates the quality of the obtained polarization angles and the definition of their uncertainties $\sigma_\varphi$ and $\sigma_\theta$. These uncertainties are defined by comparison with the theoretical backazimuth and incidence angles with $\sigma_\varphi = \pm 30°$, and $\sigma_\theta = \pm 30°$ (Fig. 10b). For simplification, all theoretical polarization angles $\varphi_{\text{calc}}$ and $\theta_{\text{calc}}$ (Fig. 10b, eq. 14) and their potential source origin times $\mathbf{T}_0$ (eqs 11–12) are calculated using a homogeneous velocity model with an expected minimum mean velocity of $V_P = 2900$ m s$^{-1}$ (Mercerat *et al.* 2010).

Misinterpretations of the incidence angles due to effects of the free surface are not taken into account during the estimation of polarization angles neither during the location procedure but are expected to be mostly smaller as compared to the assumed uncertainty $\sigma_\theta$. As shown by Neuberg & Pointer (2000), for a planar surface (as given at the study site) and small *P*-wave incidences ($<50°$), the misinterpretation of the true incidence angle from particle motion is maximally 10° but can be significant ($\sim30°$) when assuming a horizontal *P* incidence. Even though, the here assumed error $\sigma_\theta$ would even account for the extreme case of incidence angle misinterpretation, we generally excluded incidence angles larger than 50° from inversion (see below).

In addition, the choice of a homogeneous velocity model to interpret the observed polarization angles implies that we do not account for refraction effects of the Dolomite layer that strongly affect the estimated incidence angles (Figs 6d and 10b). However, the use of a more sophisticated layered velocity model would introduce a significant bias to our results, since the actual velocity structure is complex and associated with strong velocity contrasts, and which may change over time due to the developing cavity structure (Table A1). As a result, we decided to simply exclude those incidence angles from the inversion procedure that are apparently affected by refraction effects what was evaluated by the comparison to the theoretical incidence angles (Fig. 10b, Appendix). This polarization angle selection procedure is described in the following paragraph.

The estimated backazimuth angles at stations 3 and 5 show some ±180° ambiguities. Consequently, for each backazimuth angle determined from these stations, we added to the location scheme (eq. 14) an analogue angle at ±180°. At station 62, the backazimuth angle becomes erroneous for sources directly located below it, when the estimated incidence angle is $\theta = 0°$ (Fig. 10b). In these cases, the estimated backazimuth angle is excluded from the location scheme (eq. 14). The incidence angles at station 3 are completely excluded from the hypocentre location inversion, due to the presence of predominantly refracted ray paths (Figs 6 and 10b, Section 2.3). For station 5, the incidence angles with $>50°$ and estimated with respect to a *L*-value $< 0.8$ were also excluded from the inversion (Fig. 10b, Section 3.2.2).

# 4 RESULTS AND DISCUSSION

## 4.1 Relocation of the 54 classically located events

In order to estimate the performance and associated uncertainties of our location methods, we relocated all 54 selected events (Fig. 3) using (i) the probabilistic amplitude-based method $\sigma_{\text{amp}}(X, Y, Z)$ (Section 3.1), (ii) the probabilistic polarization angel-based method $\sigma_{\text{pol}}(X, Y, Z)$ (Section 3.2) and (iii) the probabilistic conjunction of the latter two $\sigma(X, Y, Z) = 1/\upsilon \, \sigma_{\text{amp}}(X, Y, Z) \, \sigma_{\text{pol}}(X, Y, Z)$ (where $\upsilon$ is a normalization constant). Fig. 11 shows examples of two good location results (events 3 and 4, Fig. 3), and two less accurate location results (events 1 and 5, Fig. 3).

For the good location results, epicentre locations are well resolved from the amplitude- and polarization-based approaches and consequently are very well resolved when using the conjunction of both methods (Fig. 11). In contrast, source depth estimations are poorly constrained using the amplitude approach, visible from the 0.34, 0.68 and 0.95 contours of the cumulative probabilities that generally cover the entire range of explored source depths. The weak constraint on source depths from this approach is generally due to the poor resolution with depth of stations used. Accurate estimates of the source depths can be partially obtained from the polarization-based approach, when backazimuth angles are available for all three stations and when reliable incidence angles are available with respect to stations 5 and 62. When combining the probability densities for both approaches, the source depth estimations are biased by the amplitude approach. The strong effect
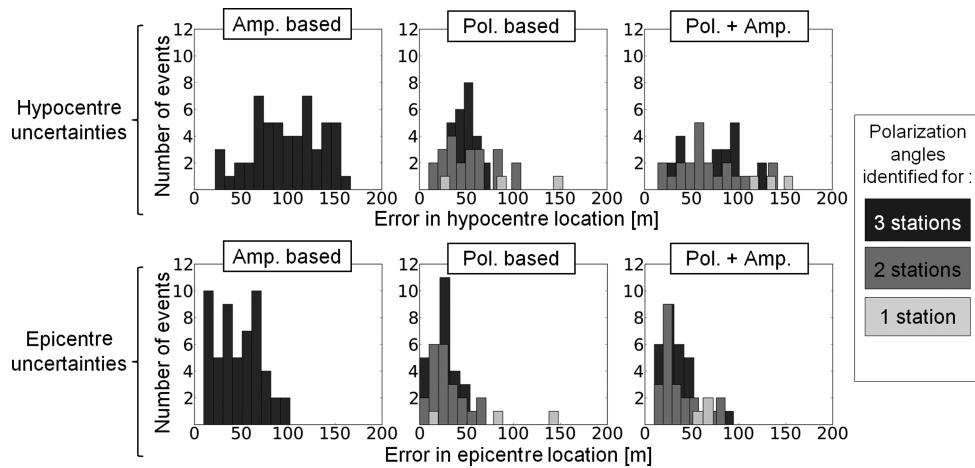
**Figure 12.** Statistics of location errors. Location errors for the 54 events using the amplitude-based, polarization-based, and the combined location approach. The errors are estimated from the absolute distance differences between the calculated hypocentre (upper panel) and epicentre (lower panel) locations and the ones obtained from the classical location approach (Fig. 3, Appendix).
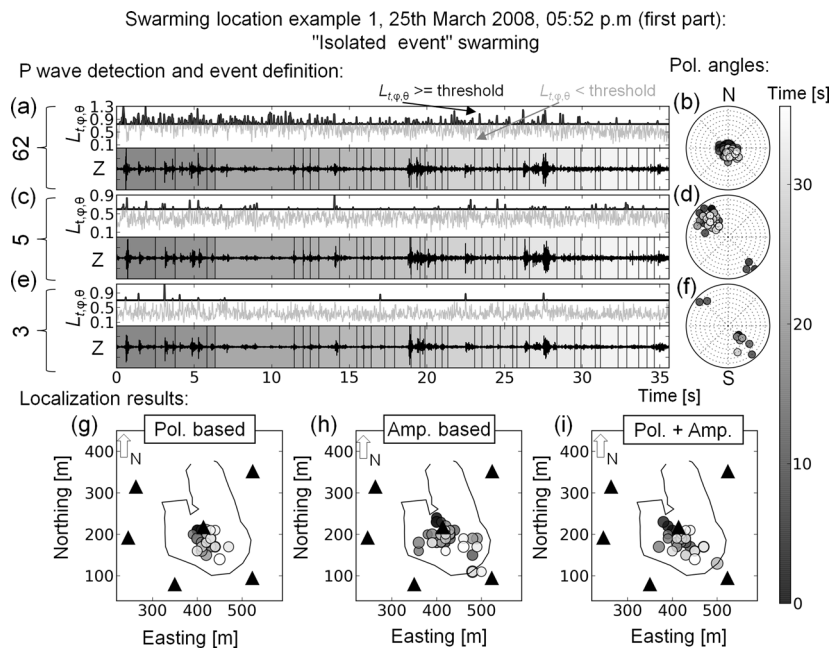


**Figure 13.** Location of an isolated event swarming sequence. Location results of swarming example 1, isolated event sequence (Fig. 2). (a, c, e) Z component traces of stations 3, 5, and 62, respectively, and the *L*-values below (grey) and above (black) the critical threshold value $L_{crit}$. Grey background colours mark the current time, and black lines denote the minimum expected source origin times $\tau^i_{start}$ for the identified events (Section 3.2.3 and Section 4.2). (b, d, f) Lower station hemisphere plots of the determined polarization angles with current time (grey scale). (Lower panels) Results for the polarization-based (g), amplitude-based (h) and combined location approaches (i).

of the amplitude-based approach on the maximum likelihood source depth estimations is related to the fact that the cumulative probabilities are spatially more extended for the polarization-based approach compared to the amplitude-approach.

A resulting deviation from the expected epicentre location is shown for event 5 using the amplitude-based approach, and for event 1 using the polarization-based approach (Fig. 11). In the case of event 5, the epicentre location error probably results from local heterogeneities at the cavity roof, leading to wave scattering effects which are not considered in our simple 1-D attenuation law (eq. 2). In the case of event 1, the epicentre location is uncertain using the polarization-based approach due to the absence of calculated polarization angles at stations 5 and 62. Local attenuation and wave scattering effects seem to be responsible for the non-determination of polarization angles at stations 5 and 62, as already discussed in Section 2.3 and Fig. 4 with respect to event 1.

Nonetheless, the shortcomings and epicentre misestimations for both location methods can be significantly improved by combining them (Fig. 11). As a result, for event 5, the shape of the 0.34 cumulative probability contour of the amplitude-based approach significantly reshapes towards the expected epicentre location when combining it with the polarization-based approach. Similarly, a well constrained epicentre location is drawn from the cumulative probabilities for event 1 upon combining both approaches.
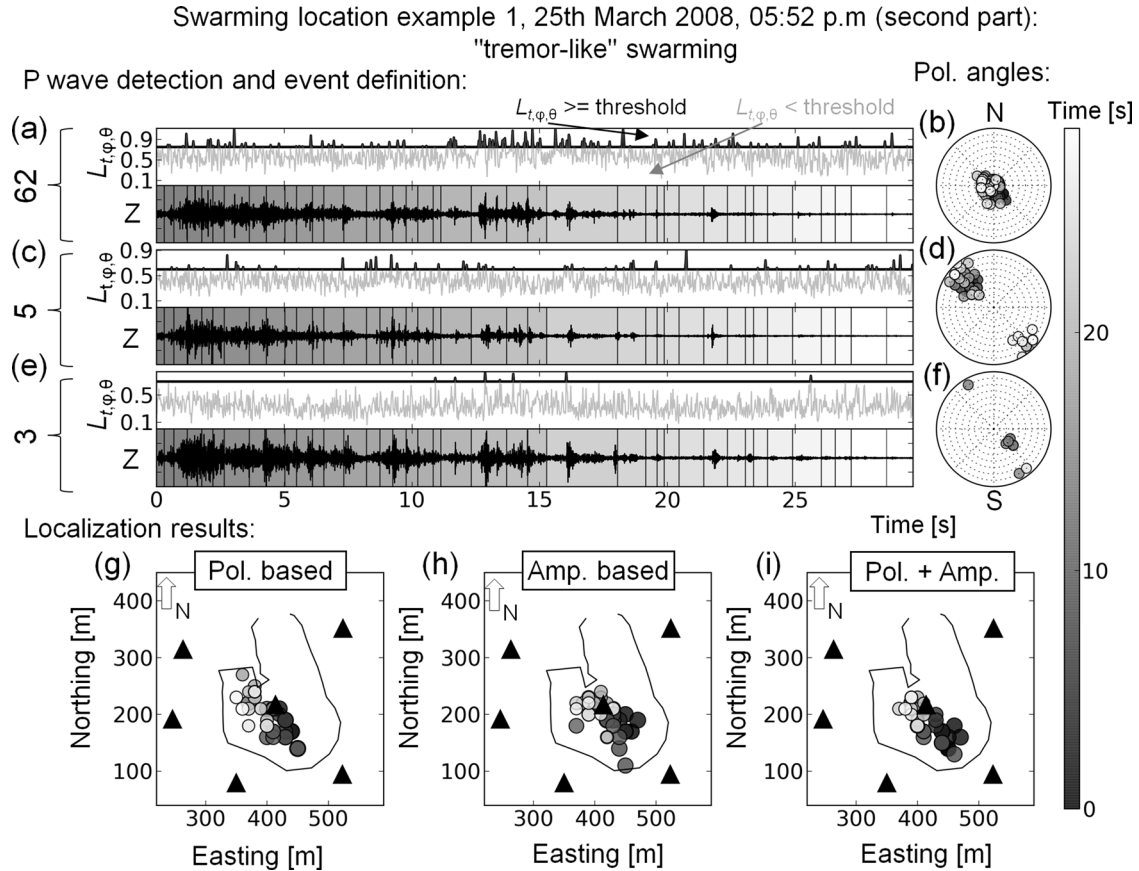
**Figure 14.** Location of a tremor-like swarming sequence. Location results of swarming example 1, tremor-like event sequence (Fig. 2). For further description see Fig. 13.

The absolute epicentre and hypocentre location errors are calculated from the distance deviations between the maximum likelihood locations obtained by our method and by the classical location approach (Fig. 3, Appendix). The absolute errors in the hypocentre locations for all 54 events are presented in Fig. 12. It should be noted that the calculated absolute errors are additionally affected by the uncertainties in the event locations calculated by the classical approach, and are of the order of $\pm 50$ m in the horizontal and even larger in the vertical coordinates, respectively (Appendix).

The absolute errors in the maximum likelihood epicentre and hypocentre locations determined by the amplitude-based approach are $< \pm 100$ m and $< \pm 160$ m, respectively (Fig. 12). For the polarization-based approach, the quality of the location results depends on the quantity of identified polarization angles at each station. The epicentre and hypocentre locations are significantly more accurate using this method, compared to the amplitude-based approach, under the circumstance that polarization angles are available for all three stations, which is the case for 51 per cent of the 54 events. For the combined approach, the epicentre errors, with at least two available stations, are significantly reduced. In contrast, as already stated above, the source depth estimations using the polarization-based approach become inaccurate when combined with the amplitude-based approach.

## 4.2 Application to swarming sequences

The two developed location approaches were applied to resolve the spatio-temporal characteristics of the observed two types of swarming sequences, isolated and tremor-like (Fig. 2). In order to identify single seismic events in isolated and tremor-like swarming sequences, we used the polarization-based *P*-wave automatic detection scheme for three-component stations 3, 5 and 62 (Section 3.2.3).

For the amplitude-based approach, the event-specific time window was defined by the minimum source origin time $\tau^i_{start}$ and the maximum source origin time $\tau^{i+1}_{end}$ of the subsequent identified event (eqs 11–13). This event window definition assures that amplitude estimates for more distant stations (e.g. 7 and 8) are always related to the entire seismic event duration, in order to determine the true event-specific maximum peak-to-peak amplitude.

In Figs 13 and 14, we show the location results for both approaches, individually and combined, for swarming sequence example 1 (Fig. 2). Consistently observed, using both location schemes, this entire swarming sequence is associated with distinct spatio-temporal epicentre migration trends. During the preceding isolated event swarming sequence, the epicentres migrate from the northwestern to the southeastern cavity region (Figs 13g–i). During the subsequent tremor-like swarming sequence, the epicentres migrate reversely from the
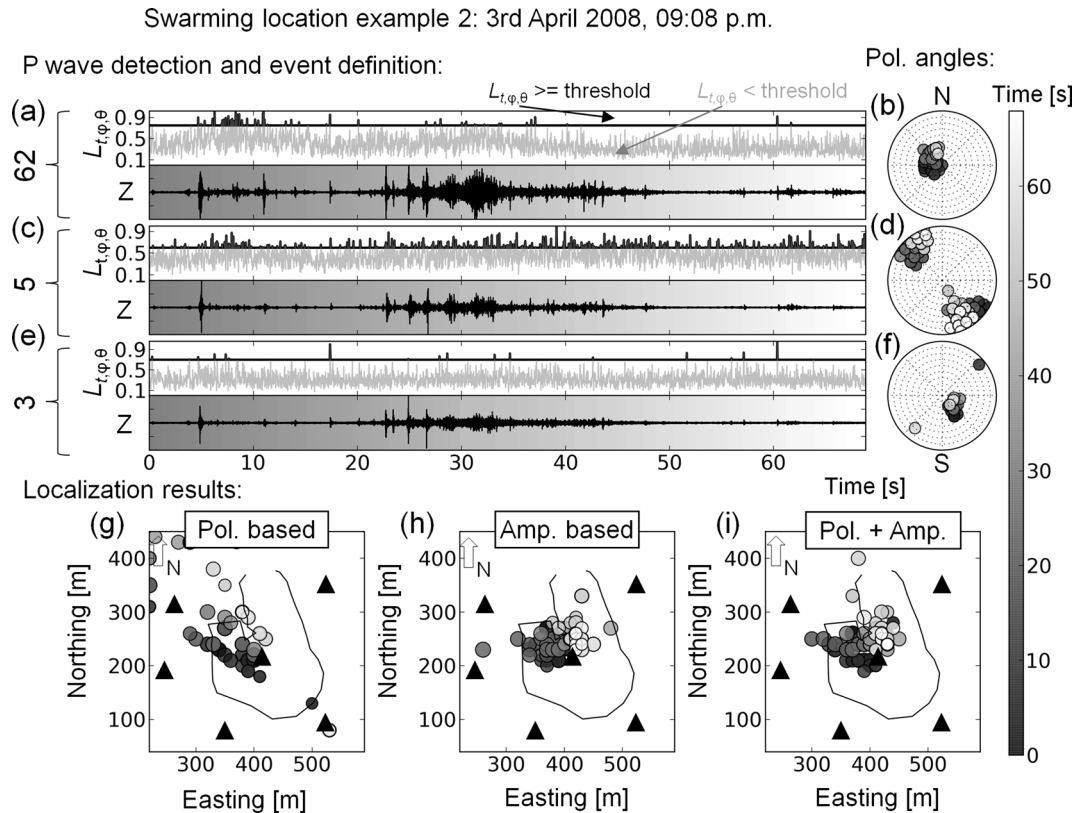
**Figure 15.** Location results for swarming sequence example 2. Further descriptions are given in Fig. 13. For a better illustration, the minimum expected source origin times $\tau^i_{\text{start}}$ of the identified events are not shown here.

southeastern to the northwestern cavity region (Figs 14g–i). These cyclic spatio-temporal epicentre migrations are clearly identified at stations 5 and 62 by the calculated back azimuth and incidence angles (Figs 13b, d and 14b, d). In contrast, the exact dimension of the epicentre migration trends cannot be completely resolved using our approach, due to the significant uncertainties in the epicentre locations, averaging around ±50 m (Fig. 12). For both swarming sequences, hypocentre depths are poorly resolved and very noisy, and hence, are not shown in the figures.

Similarly, distinct spatio-temporal epicentre migrations are observed for two other main swarming sequences, namely examples 2 (Fig. 15) and 3 (Fig. 16). For the swarming sequence example 2, cyclic epicentre migration trends are observed with an initial migration direction towards the west and a subsequent migration towards the east (Fig. 15). However, for both swarming sequence examples 2 and 3, the locations for the tremor-like event sequences are related to bigger uncertainties due to the lack of polarization angles available at station 62 (Figs 15 and 16). The quantity of *P*-wave detections at this station decreases significantly, as *P*-wave onsets are widely covered by the coda of the preceding event and by the general increase in the high frequency noise level associated with comparatively stronger and more frequent seismic energy releases (Figs 15a and 16a). On the other hand, *P* waves are frequently detected at the more distant station 5, where high frequency noise widely vanishes due to attenuation (Figs 15c and 16c).

The amplitude-based location approach appears generally robust for the tremor-like event sequences, however remains more sensitive to isolated event sequences when these are associated with close concatenations of individual events that strongly vary in amplitude (Fig. 13). In these cases, the amplitudes estimated at each station can be related to different isolated events, leading to erroneous locations when the amplitudes of the different events vary significantly. Such an effect and limitation are visible from the more scattered nature of located events using the amplitude-based approach (Fig. 13h), compared to the polarization-based (Fig. 13g) or combined approaches (Fig. 13i).

### 4.3 Application to the 2008 microseismic crisis: preliminary insights into caving dynamics

#### 4.3.1 Principal observations

The automatic event identification and location approaches used for the swarming sequences (Figs 13–16) are applied to the entire data set of the 2008 microseismic crisis (Fig. 17a). The microseismic activity is characterized by three distinct periods, marked by cascade-like increasing peaks in seismic activity and subsequent periods of quiescence. The third period of activity represents the main shock, and is associated with two major seismic activity peaks on the 3rd and 4th of April 2008, at 9 p.m. and 8 a.m., respectively. These peaks correspond to the swarming sequence examples 2 and 3, respectively (Figs 15 and 16).
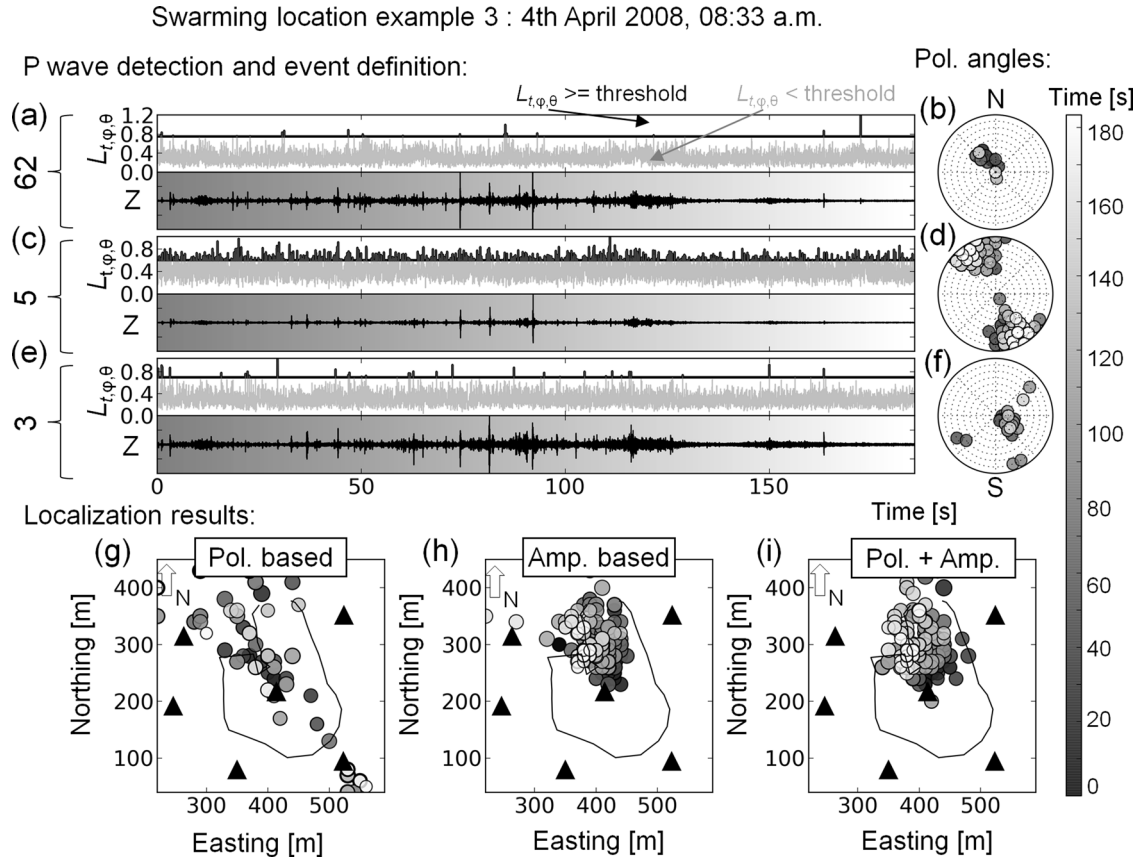
**Figure 16.** Location results for swarming sequence example 3. Further descriptions are given in Fig. 13. For better illustration, the minimum expected source origin times $\tau^i_{\text{start}}$ of the identified events are not shown here.

Following this distinct temporal microseismic distribution, clusters of epicentre locations clearly display spatio-temporal migrations for different time windows during the microseismic crisis (Fig. 17). These migrations occur within a few hours (e.g. Figs 17d and i), days (Figs 17b–c, e, g–h) and weeks (Fig. 17f). Comparing the epicentre locations for these different time windows and periods, an apparent N–N–W to S–S–E migration and vica versa is observed. In addition, the epicentre locations show a long-term northward migration from the 14th of March 2008 to the final peak in activity happening on the 4th of April 2008 (Figs 17b–h).

Fig. 18 shows the apparent spatio-energetic distribution of the 2008 microseismic crisis, based on the maximum likelihood locations obtained from the polarization-based (Fig 18a) and the combined approach (Figs 18b and c). As stated in Section 4.1, the polarization-based approach provides better location results for the source depths, while the combined approach provides better epicentre location resolution (Fig. 11). The apparent seismic energy $E$ for each gridpoint ($\mathbf{X}$, $\mathbf{Y}$, $\mathbf{Z}$) was approximated by

$$E\left(\mathbf{X}, \mathbf{Y}, \mathbf{Z}\right) = \log_{10}\left[N\left(\mathbf{X}, \mathbf{Y}, \mathbf{Z}\right) \cdot A^2\left(\mathbf{X}, \mathbf{Y}, \mathbf{Z}\right)\right], \tag{17}$$

where $N$ is the number of events, $A$ the peak-to-peak amplitude estimated from station 62 for the frequency band 30–90 Hz and corrected for attenuation by multiplying $r^{-1.7}$ (Table 1), where $r$ is the epicentral distance. Seismic events with amplitudes below an apparent magnitude of completeness ($\sim$50 per cent) are excluded from the distribution shown in Fig. 18. The apparent magnitude of completeness was defined by finding the amplitude bin with the highest number (frequency) of events identified from a frequency-amplitude plot.

The spatio-energetic distribution as a function of depth, shown in Fig. 18(a), marks very well the vertically evolved cavity roof measured after the crisis by sonar measurements (Fig. 1). Even the asymmetry in the vertical roof extension between the eastern and the western part of the cavity zones is reproduced (Fig. 18a). The spatio-energetic distribution in the horizontal plane, as seen from Fig. 18(b), clearly agrees with the lateral extensions of the cavity zone. Also, microseismicity nicely redraws the asymmetric shape of the cavity associated with a larger N–S extension along the eastern side, compared to the western side. The major seismogenic zone, as marked by the maximum of released microseismic energy, is found in the transition zone lying between the highest cavity roof extension to the E–S–E and the lower cavity roof extension to the W–N–W.

Fig. 18(c) shows the cumulative seismic energy along the two exploitation profiles in comparison with the cavity roof growth obtained by sonar measurements realized before and after the microseismic crisis in 2008 February and May, respectively. From this illustration it can be clearly seen that the amount of cumulative seismic energy increase almost proportionally with the respect to the size of collapsed cavity roof portions during the crisis in 2008. Accordingly, the largest cavity roof collapse was measured at the northern cavity zone along profile A which agrees with the location of maximum cumulative seismic energy.
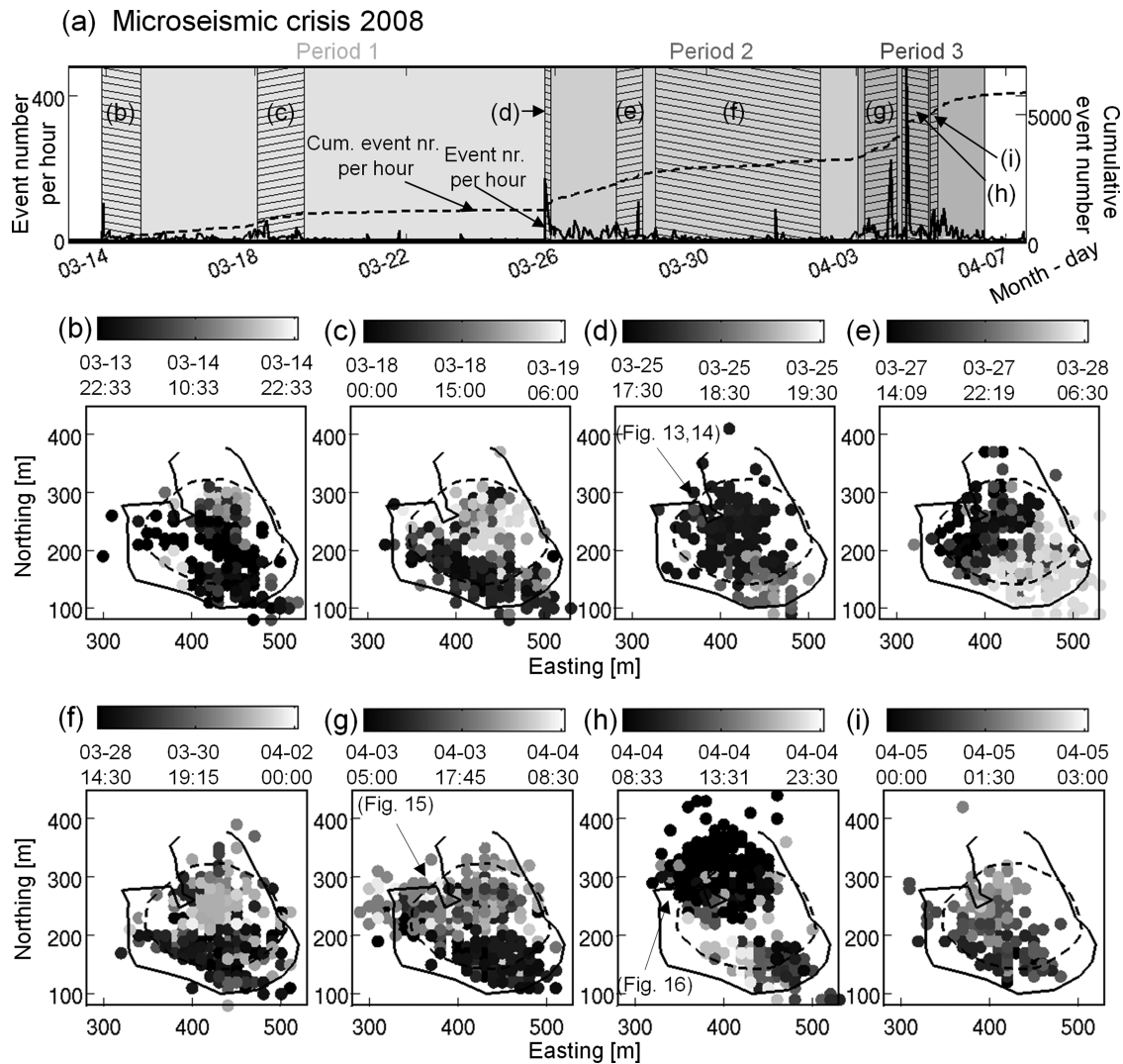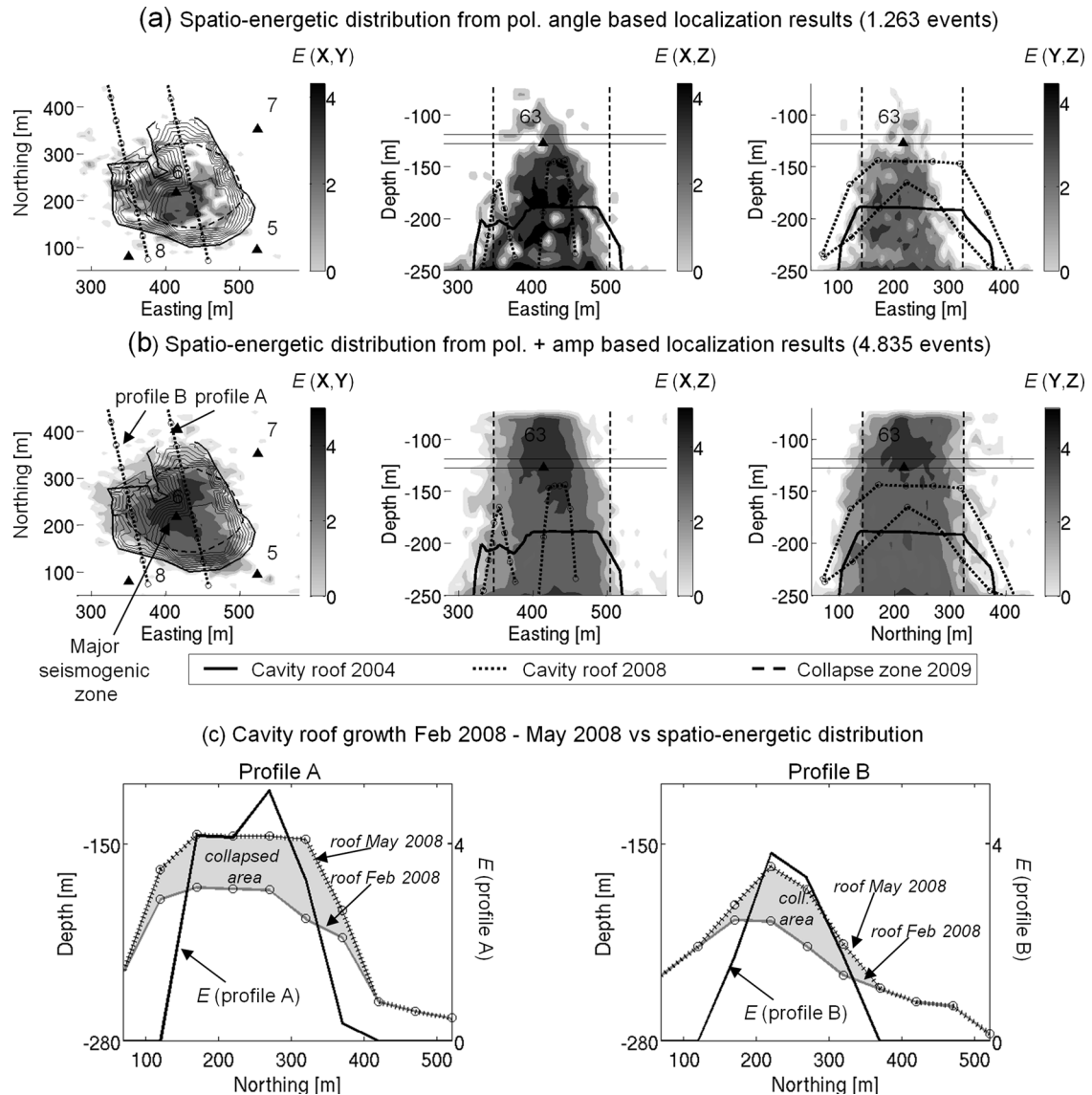
**Figure 17.** Location results of the microseismic crisis in 2008. (a) Seismic activity of the 2008 microseismic crisis, detected and located by the polarization-based and amplitude-based approaches (Section 3.2), and associated with amplitudes greater than an apparent magnitude of completeness (Section 4.3.1). The number of seismic events per hour (continuous black line) and the cumulative event number (dashed black line) indicate three distinct periods of seismic activities (grey shaded areas). (b–i) Spatio-temporal epicentre distribution with respect to selected time windows [areas textured with black lines in (a)] for each period of activity.

### 4.3.2 Preliminary interpretation of the microseismicity

Taking into account all our results and observations, we think that the microseismicity generated at the Cerville-Buissoncourt salt mine cavity generally represents rock detachment cracking and breakage processes along the cavity roof. Accordingly, microseismic activity is concentrated to zones where the cavity structure has significantly evolved during the crisis in 2008 (Fig. 18). In addition, as stated in Section 2.2, the release of seismic energy through the brine-filled cavity by impacts of rock falls on the cavity bottom is unlikely. As a result, the microseismicity located inside the cavity structure must be interpreted as poorly resolved source depth location (Fig. 18a). Very similar signals to our swarming sequences were reported for microseismic studies of detachment and block fall processes linked with unstable rock slopes (Mertl & Bruckl 2007; Spillmann *et al.* 2007; Levy *et al.* 2010). These studies reported so called 'multiple' microearthquakes which agree in signal duration and signature with our microseismic data.

Moreover, we suggest that the isolated microseismic events represent detachment cracking associated with a rupture mode 1 with a vertical axis as indicated by our results on the S–P amplitude ratios (Fig. 6, Section 2.3). In addition, dip slip faulting modes seems to be included in the mechanisms of cavity roof deformation too as observed from significant *SH*-wave amplitudes for isolated events at station 3 (Fig. 10a, Section 3.2.2). Nonetheless, in this study we cannot give a rigorous assessment with respect the governing mechanisms which will be the scope of future detailed source analysis.

The spatio-temporal epicentre migrations associated with the swarming examples (Figs 13–16) indicate, that both, isolated and tremor-like swarming sequences clearly interact with each other, maybe in a way that isolated local detachment cracks initiate a self-reinforcing chain reaction which forms a failure zone, succeeded by rock breakage. The most noticeable event of such chain reaction cavity roof failure

(a) Spatio-energetic distribution from pol. angle based localization results (1.263 events)

(b) Spatio-energetic distribution from pol. + amp based localization results (4.835 events)

———— Cavity roof 2004      ·········· Cavity roof 2008      – – Collapse zone 2009

(c) Cavity roof growth Feb 2008 - May 2008 vs spatio-energetic distribution

**Figure 18.** Spatio-energetic distribution of the 2008 microseismic crisis, representing the apparent seismic energy $E$ (eq. 17, see Section 4.3.1) calculated for the largest seismic events (see Section 4.3.1) located using polarization angles from all three stations 3, 5 and 62, and incidence angles $<50°$ at station 5 (a), using the combined location approach with polarization angles available for at least two stations for one seismic event (b). (c) Cavity roof growth during the crisis in 2008 (left ordinate) and the cumulative energy $E$ calculated along two profiles A and B (a, Fig. 1). The collapsed area of the cavity roof (grey shaded area) is represented by the difference between to sonar measurements (black circles) along the two profiles obtained before and after the microseismic crisis 2008, in 2008 February and May, respectively.

is represented by the distinct northward epicentre migration happening on the 4th of April 2008 (Fig. 17h) associated with the swarming example 3 (Fig. 16). At the same time of this major microseismic swarming activity a significant increase in the brine pressure level was measured at the exploitation wells located about 1 km to the north of the cavity structure (Fig. 1, Klein *et al.* 2008). This observation indicates that the observed swarming activity might represent the major collapse of the northern cavity roof as shown by the sonar measurements shown in Fig. 18(c).

The fact that spatio-temporal epicentre migrations occur on different time-scales and cover laterally larger areas of the total cavity zone (Figs 13–17) indicates that the triggering mechanism for detachments and rock failures are probably related to processes of bulk stress accommodation and redistribution. Generally, the cavity roof is supposed to be in a critical state of stress, and the partial release of stress in one zone provokes stress concentrations and subsequent failures in adjacent zones, and vice versa. A major factor in these stress redistribution processes might be seen in the distinct relief of the cavity roof. Accordingly, the major seismogenic zone is located in the transition zone between the highest cavity extension to the S–S–E and the lowest to the N–N–W (Fig. 18b) which might be a key zone prone to the initiation of cavity roof failure.

However, it is beyond the scope of this paper to explain and examine the mechanics and systematic dynamics of the observed caving processes. Future research will be carried out in order to completely understand the origin(s) of these spatio-temporal microseismic

characteristics by means of further detailed quantitative and qualitative analyses and comparisons with the other explored geophysical parameters (e.g. Cao *et al.* 2010; Contrucci *et al.* 2011). Therein, one possible approach in future work might be the comparison of high-frequency locations of this study with results from broadband data analysis. Interestingly, Jousset & Francois (2008) observed ultralong signals on local broad-band station that were so far interpreted as possible tilt effects on the seismometer due to ground relaxation after larger block falls from the cavity roof, what was consistently recorded on local tachymetric, and GPS data sets (Klein *et al.* 2008; Daupley *et al.* 2013) and might be now quantified by comparison with the method and results obtained in from this study.

# 5 CONCLUSIONS AND OUTLOOK

This paper presents two probabilistic location approaches that resolve the spatio-temporal characteristics of complex swarming sequences recorded in a growing cavity environment, at a local-scale. The presented methods take advantage of the dominance in *P*-wave energies at high frequencies ($>100$ Hz). In the first approach, location is based on peak-to-peak amplitudes and an attenuation model, while the second approach is designed to detect significantly polarized high frequency *P*-wave energies and their associated polarization angles. From both methods epicentre locations are resolved ($\sim \pm 50$ m), while accurate source depth determinations are only provided for particular cases from the polarization-based approach.

Microseismicity seems to mainly represent detachment and breakage processes along the cavity roof, compatible to the reported evolution of the cavity roof. In addition, we observed clear spatio-temporal migration in epicentre locations over different time scales (from seconds to days) located along the entire cavity roof, as diagnostic of chain reaction failures.

Future research needs to be performed in order to better understand the governing physical dynamics for the observed microseismicity. In this regard, our location results and observations on the microseismic signal characteristics should be examined in combination with local geophysical data sets (such as geodetic deformation measurements) which are under examination. Furthermore, our interpretation of the origin of the microseismicity and its spatio-temporal changes would be greatly improved with the incorporation of more accurate source depth determinations, as in particular by the incorporation of seismogram records of stations 62 and 63.

## REFERENCES

Aki, K. & Richards, P.G., 2002. *Quantitative Seismology*, 2nd edn. University Science Books.

Battaglia, J. & Aki, K., 2003. Location of seismic events and eruptive fissures on the Piton de la Fournaise volcano using seismic amplitudes, *J. geophys. Res.*, **108**, 10–1029.

Battaglia, J., Aki, K. & Ferrazzini, V., 2005. Location of tremor sources and estimation of lava output using tremor source amplitude on the Piton de la Fournaise volcano: 1. Location of tremor sources, *J. Volcan. Geotherm. Res.*, **147**(3–4), 268–290.

Beyreuther, M., Barsch, R., Krischer, L., Megies, T., Behr, Y. & Wassermann, J., 2010. ObsPy: a Python toolbox for seismology, *Seism. Res. Lett.*, **81**, 530–533.

Brune, J.N., 1970. Tectonic stress and the spectra of seismic shear waves from earthquakes, *J. geophys. Res.*, **75**, 4997–5009.

Campillo, M., Bouchon, M. & Massinon, B., 1984. Theoretical study of the excitation, spectral characteristics, and geometrical attenuation of regional seismic phases, *Bull. seism. Soc. Am.*, **74**, 79–90.

Cao, N.-T., Klein, E., Contrucci, I., Daupley, X. & Bigarre, P., 2010. Large-scale salt cavern collapse: multi-parameter monitoring from precursor signs to general failure, in *Rock Mechanics in Civil and Environmental Engineering (EUROCK 2010)*, pp. 709–712, eds Zhao, J., Labiouse, V., Dudt, J.-P. & Mathier, J.-F., CRC Press.

Caramanna, G., Ciotoli, G. & Nisio, S., 2008. A review of natural sinkhole phenomena in Italian plain areas, *Nat. Hazards*, **45**(2), 145–172.

Contrucci, I., Klein, E., Cao, N.T., Daupley, X. & Bigarre, P., 2011. Multi-parameter monitoring of a solution mining cavern collapse: first insight of precursors, *Comptes Rendus Geosci.*, **343**, 1–10.

Dahm, T., Heimann, S. & Bialowons, W., 2011. A seismological study of shallow weak micro-earthquakes in the urban area of Hamburg city, Germany, and its possible relation to salt dissolution, *Nat. Hazards*, **58**, 1111–1134.

Daupley, X., Cuche, H. & Ghoreychi, M., 2005. Typology of strata movement related to old solution mining of salt at Sarralbe (Lorraine, France), in *Proceedings of the Post-Mining 2005*, November 16–17, Nancy, France, 13 pp.

Daupley, X. *et al.*, 2010. Multiparameter monitoring of a salt cavern collapse (Cerville-Buissoncourt site, France), in *Proceedings of the EGU General Assembly Conference Abstracts*, Vol. 12, p. 1240.

Daupley, X., Laouafa, F. & Contrucci, I., 2013. L'effondrement de la cavité saline de Cerville-Buissoncourt—analyse des mécanismes conduisant à l'effondrement: Dans manuel de mécanique des roches, *Tome III: Retours d'expériences - Génie minier et pétrolier*, pp. 59–69, ed. Pierre, Duffaut.

Di Grazia, G., Falsaperla, S. & Langer, H. 2006. Volcanic tremor location during the 2004 Mount Etna lava effusion, *Geophys. Res. Lett.*, **33**, L04304, doi:10.1029/2005gl025177.

Duplancic, P. & Brady, B.H., 1999. Characterisation of caving mechanisms by analysis of seismicity and rock stress, in *Proceedings of the 9th Congress International Society for Rock Mechanics*, Vol. 2, pp. 1049–1053, eds Vouille, G. & Beres, P., Balkema.

Flinn, E.A., 1965. Signal analysis using rectilinearity and direction of particle motion, *Proc. IEEE*, **53**, 1874–1876.

Gibowicz, S.J., 2009. Seismicity induced by mining: recent research, *Adv. Geophys.*, **51**, 1–53.

Glazer, S.N. & Hepworth, N., 2005. Seismicity induced by cave mining, Palabora experience, in *Proceedings of 6th International Symposium*

on *Rockbursts and Seismicity in Mines*, pp. 281–289, eds Potvin, Y. & Hudyma, M., ACG, Perth.

Gutierrez, F., Cooper, A.H. & Johnson, K.S., 2008. Identification, prediction, and mitigation of sinkhole hazards in evaporite karst areas, *Environ. Geol.*, **53**(5), 1007–1022.

Hasegawa, H.S., Wetmiller, R.J. & Gendzwill, D.J., 1989. Induced seismicity in mines in Canada—an overview, *Pure appl. Geophys.*, **129**, 423–453.

Hudyma, M. & Potvin, Y.H., 2010. An engineering approach to seismic risk management in hardrock mines, *Rock Mech. Rock Eng.*, **43**, 891–906.

Jolly, A.D., Thompson, G. & Norton, G.E., 2002. Locating pyroclastic flows on Soufriere Hills Volcano, West Indies, using amplitude signals from high dynamic range instruments, *J. Volc. Geotherm. Res.*, **118**, 299–317.

Jones, G.A., Kulessa, B., Doyle, S.H., Dow, C.F. & Hubbard, A., 2013. An automated approach to the location of icequakes using seismic waveform amplitudes, *Ann. Glaciol.*, **54**, 1–9.

Jousset, P. & Francois, B., 2008. Surveillance sismologique large bande pour l'après-mine: installation d'un réseau à Cerville-Buissoncourt, Rapport BRGM/RP- 56727-FR, 35, p. 10 ill.

Jousset, P. & Rohmer, J., 2012. Evidence for remotely triggered microearthquakes during salt cavern collapse, *Geophys. J. Int.*, **191**, 207–223.

Klein, E., Contrucci, I., Daupley, X., Hernandez, O., Bigarre, P., Nadim, C., Cauvin, L. & Pierson, M., 2008. Experimental monitoring of a solution-mining Cavern in Salt: identifying and analyzing early-warning signals prior to collapse, in *Proceedings of the SMRI Fall 2008 Technical Conference*, pp. 135–146. SMRI Galveston (Austin), TX, USA.

Kosecki, A., Piwakowski, B. & Driad-Lebeau, L., 2010. High resolution seismic investigations in salt mining context, *Acta Geophys.*, **58**, 15–33.

Kwiatek, G. & Ben-Zion, Y., 2013. Assessment of P and S wave energy radiated from very small shear-tensile seismic events in a deep South African mine, *J. geophys. Res.*, **118**, 3630–3641.

Lay, T. & Wallace, T.C., 1995. *Modern Global Seismology*, Academic Press.

Lebert, F., Bernardie, S. & Mainsant, G., 2011. Hydroacoustic monitoring of a salt cavity: an analysis of precursory events of the collapse, *Nat. Hazards Earth Syst. Sci.*, **11**, 2663–2675.

Levy, C., Baillet, L., Jongmans, D., Mourot, P. & Hantz, D., 2010. Dynamic response of the Chamousset rock column (Western Alps, France), *J. geophys. Res.*, **115**, 2003–2012.

Li, T., Cai, M.F. & Cai, M., 2007. A review of mining-induced seismicity in China, *Int. J. Rock Mech. Min. Sci.*, **44**, 1149–1171.

Malovichko, D., Dyagilev, R., Shulakov, D.Y. & Butyrin, P., 2009. Seismic monitoring of large-scale karst processes in a potash mine, in *Controlling Seismic Hazard and Sustainable Development of Deep Mines*, pp. 989–1002, ed. Tang, C.A., Rinton Press.

Malovichko, D.A., Kadebskaya, O.I., Shulakov, D.Y. & Butyrin, P.G., 2010. Local seismologic observations of karst processes, *Phys. Solid Earth*, **46**, 57–73.

McNutt, S.R., 1992. Volcanic tremor, *Encycloped. Earth Syst. Sci.*, **4**, 417–425.

Mendecki, A.J., 1996. *Seismic Monitoring in Mines*, Chapman & Hall.

Mercerat, E.D., 2007. Sismicité induite et modélisation numérique de l'endommagement dans un contexte salin. *PhD thesis*, LAEGO Institut National Polytechnique de Lorraine, France (in French).

Mercerat, E.D., Driad-Lebeau, L. & Bernard, P., 2010. Induced seismicity monitoring of an underground salt cavern prone to collapse, *Pure appl. Geophys.*, **167**, 5–25.

Mertl, S. & Bruckl, E., 2007. Observation of fracture processes in creeping rock masses by seismic monitoring, in *Proceedings at 11th Congress of the International Society for Rock Mechanics*, Lisbon, Portugal.

Neuberg, J. & Pointer, T., 2000. Effects of volcano topography on seismic broad-band waveforms, **143**, 239–248.

Nothnagel, R., 2003. Modélisation des instabilités en Mécanique des Roches: application à l'exploitation de la concession de Drouville, *PhD thesis*, Ecole des Mines de Paris, Paris, France (in French).

Plesinger, A., Hellweg, M. & Seidl, D., 1986. Interactive high-resolution polarization analysis of broadband seismograms, *J. Geophysics*, **59**, 129–139.

Senfaute, G., Chambon, C., Bigarre, P., Guise, Y. & Josien, J.P., 1997. Spatial distribution of mining tremors and the relationship to rockburst hazard, *Pure appl. Geophys.*, **150**, 451–459.

Sethian, J.A., 1999. Fast marching methods, *SIAM Rev.*, **41**, 199–235.

Spillmann, T., Maurer, H., Green, A. G., Heincke, B., Willenberg, H. & Husen, S., 2007. Microseismic investigation of an unstable mountain slope in the Swiss Alps, *J. geophys. Res.*, **112**, B07301, doi:10.1029/2006JB004723.

Taisne, B., Brenguier, F., Shapiro, N.M. & Ferrazzini, V., 2011. Imaging the dynamics of magma propagation using radiated seismic intensity, *Geophys. Res. Lett.*, **38**, L04304, doi:10.1029/2010GL046068.

Tarantola, A., 2005. *Inverse Problem Theory and Methods for Model Parameter Estimation*, SIAM.

Tarantola, A. & Valette, B., 1982. Inverse problems = quest for information, *J. Geophys.*, **50**, 159–170.

Trifu, C.I. & Shumila, V., 2010. Microseismic monitoring of a controlled collapse in field II at Ocnele Mari, Romania, *Pure appl. Geophys.*, **167**, 27–42.

Urbancic, T.I. & Trifu, C.I., 2000. Recent advances in seismic monitoring technology at Canadian mines, *J. appl. Geophys.*, **45**, 225–237.

Warpinski, N., 2009. Microseismic monitoring: inside and out, *J. Petrol. Technol.*, **61**, 80–85.

Whyatt, J. & Varley, F, 2008. Catastrophic failures of underground evaporite mines, in *Proceedings 27th International Conference on Ground Control in Mining*, 2008 July 29–31, Morgantown, West Virginia, pp. 29–31.

Wuestefeld, A., Kendall, J.M., Verdon, J.P. & Van As, A., 2011. In situ monitoring of rock fracturing using shear wave splitting analysis: an example from a mining setting, *Geophys. J. Int.*, **187**, 848–860.

Wust-Bloch, G.H. & Joswig, M., 2006. Pre-collapse identification of sinkholes in unconsolidated media at Dead Sea area by nanoseismic monitoring (graphical jackknife location of weak sources by few, low-SNR records), *Geophys. J. Int.*, **167**, 1220–1232.

Yamasato, H., 1997. Quantitative analysis of pyroclastic flows using infrasonic and seismic data at Unzen Volcano, Japan, *J. Phys. Earth*, **45**, 397–416.

Young, R.P., Maxwell, S.C., Urbancic, T.I. & Feignier, B., 1992. Mining-induced microseismicity: monitoring and applications of imaging and source mechanism techniques, *Pure appl. Geophys.*, **139**, 697–719.

Zang, A., Oye, V., Jousset, P., Deichmann, N., Gritto, R., McGarr, A., Majer, E. & Bruhn, D., 2014. Analysis of induced seismicity in geothermal reservoirs—an overview, *Geothermics*, **52**, 6–21.

Zhu, T., Chun, K.Y. & West, G.F., 1991. Geometrical spreading and Q of Pn waves: an investigative study in eastern Canada, *Bull. seism. Soc. Am.*, **81**, 882–896.

## APPENDIX: RESULTS FROM CLASSICAL EVENT LOCATION

A total of 54 isolated events were carefully examined with respect to their hypocentre locations (Fig. 3). In our hypocentre inversion, we have chosen a classical probabilistic approach (Tarantola & Valette 1982; Tarantola 2005) based on the minimization of observed and calculated *P*-wave arrival time differences (for all network stations), *P* minus *S* arrival times, as well as polarization angles (for three-component stations) following Mercerat (2007), Mercerat *et al.* (2010), and Contrucci *et al.* (2011). Polarization angles were carefully determined from direct *P*-wave onsets using the conventional eigenanalysis of the seismic data matrix (e.g. Flinn 1965) at lower frequencies than <100 Hz, and with polarization angle uncertainties lying around ±20°. Picking errors for *P* and *S* wave arrival times laid around ±0.03 and ±0.05 s, respectively. The model space sampling for our hypocentre inversion was defined by a grid search for a 10 m × 10 m × 10 m grid, and over the coordinate

**Table A1.** Elastic characteristics for the major geological units (Fig. 1, Section 2.1) estimated from laboratory analysis and calibration shots, as carried out by Mercerat (2007), Mercerat *et al.* (2010) and Nothnagel (2003).

| Geological layers | Depth (m) | $V_p$ (km s$^{-1}$) | $V_P/V_S$ | Density (g cm$^{-3}$) |
|---|---|---|---|---|
| Marls and sands | 0–119 | 2.4–3.0 | 1.83 | 2.5 |
| Dolomite | 119–127.5 | 5.0 | 1.73 | 2.89 |
| Anhydritic marls | 127.5–183.5 | 4.0 | 1.83 | 2.657 |
| Salt | >183.5 | 4.2 | 1.8 | 2.15 |
| Brine filled cavity | Fig. 1 | 1.5 | | 1.0 |

system X = 220–580 m, Y = 40–450 m and Z = –(250–50) m (Fig. 1). We used the fast marching method (e.g. Sethian 1999) implemented in a Matlab code (provided by the website https://sites.google.com/site/patricknraanespro/fast-marching-method) in order to calculate ray paths and body wave arrival times for each source–receiver paths based on a 2-D velocity model taking into account the true cavity geometry for each station-source path way (Figs 1 and 3). As a result, compared to a 1-D model we generally account for the 2-D vertical extension of the cavity structure with respect to the direct station-source path way. On the other hand, we do not account for lateral pathways introduced by the 3-D cavity structure but we are dealing with lower computation times than when using a complete 3-D velocity model. The layers of the velocity model and the associated *P*- and *S*-wave velocities are shown in Table A1.

Epicentre locations are generally well resolved, with errors in the horizontal coordinates of <±50 m, while slightly bigger uncertainties describe the northern and eastern parts of the cavity zone due to the lack in receiver coverage (Fig. 1). Errors in location correspond to the maximum distance between the maximum-likelihood location and the most distant location of all locations covered by the 0.68 cumulative probability function. It must be stressed that the resolution of our epicentre locations is widely controlled by the information on the polarization angles (station backazimuths). The inversion of traveltime differences for this study site, is often ill-posed, as the observed picking errors are generally too high with respect to the observed traveltime differences. This problem arises from the combination of short hypocentral distances (50–300 m) with comparatively fast seismic velocities (up to 5000 m s$^{-1}$; Table A1). Assuming a much lower mean velocity of 2500 m s$^{-1}$, then the expected maximum traveltimes will be 0.12 s, which is only 12 times bigger than the picking error.

Source depths are associated with a larger uncertainty and should be regarded with caution. These larger uncertainties are mainly due to the limited resolution in depth of the microseismic network. Potentially, best constraints on source depths can be found from traveltime differences observed at the central borehole stations 63 and 62. However, phase picking at station 63 is complicated (Section 2.3), so that picking errors are often in the same range as the observed traveltime differences. Resolving source depths from polarization incidence angles and ray path modelling is impeded by predominant refracted wave travels through the Dolomite layer (Fig. 6a). Consequently, the observed incidence angles are often close to horizontal at station 63 and around a constant critical angle of refraction (between the Dolomite and the overlying Marl layers) at station 3 (Fig. 6d). The modelling of these refracted ray paths, with respect to source depths, depends strongly on the velocity model used, and may bias the results, since the velocity structure and contrasts between the cavity roof and the overlying Marl and Dolomite layers are supposed to be very complex and involve temporal changes due to the evolution of the cavity roof. Direct ray paths are generally observed at station 62, as demonstrated by the observed small incidence angles, which generally provide the most valuable information on source depths.